One-dimensional nanostructured electrocatalysts for polymer electrolyte membrane fuel cells-a review

Lu, Yaxiang; Du, Shangfeng; Steinberger-Wilckens, Robert

DOI:
10.1016/j.apcatb.2016.06.022

Title: One-dimensional nanostructured electrocatalysts for polymer electrolyte membrane fuel cells-a review

Author: Yaxiang Lu Shangfeng Du Robert Steinberger-Wilckens

PII: S0926-3373(16)30460-X
DOI: http://dx.doi.org/doi:10.1016/j.apcatb.2016.06.022
Reference: APCATB 14846

To appear in: *Applied Catalysis B: Environmental*

Received date: 11-4-2016
Revised date: 3-6-2016
Accepted date: 6-6-2016

Please cite this article as: Yaxiang Lu, Shangfeng Du, Robert Steinberger-Wilckens, One-dimensional nanostructured electrocatalysts for polymer electrolyte membrane fuel cells-a review, Applied Catalysis B, Environmental http://dx.doi.org/10.1016/j.apcatb.2016.06.022

One-dimensional nanostructured electrocatalysts for polymer electrolyte membrane fuel cells-a review

Yaxiang Lu, Shangfeng Du, Robert Steinberger-Wilckens*

School of Chemical Engineering, University of Birmingham, Edgbaston, Birmingham B15 2TT, UK

To whom correspondence should be addressed to:

*SF Du: E-mail: s.du@bham.ac.uk, Tel: +44-121-4158696

Graphical abstract

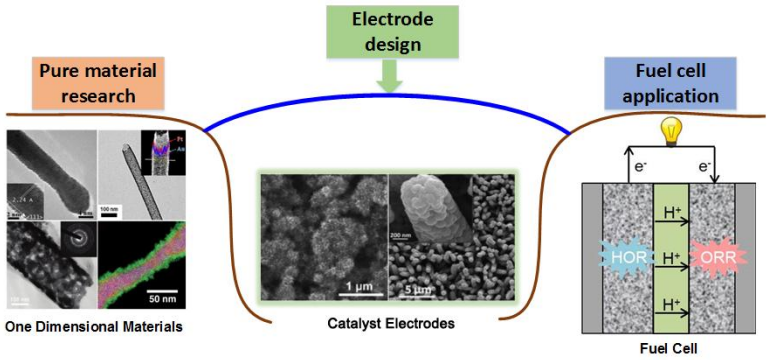

Highlights

- Reviewing recent five years' work on one-dimensional (1D) nanostructured electrocatalysts
- Focusing on the application in oxygen reduction and hydrocarbon oxidation reactions for PEMFCs
- Covering 1D Pt-based, non-Pt precious metal and non-precious metal catalysts (NPMCs)
- Summarizing the performance via ex-situ electrochemical measurement as well as in-situ fuel cell testing
- Providing critical perspectives for bridging the gap between pure material research and fuel cell development

Abstract

Recent research on one-dimensional (1D) nanostructured materials brings in tremendous progress on their application as catalysts in polymer electrolyte membrane fuel cells (PEMFCs). The desired 1D nanomaterials with tailored morphology, structure and composition can potentially address many drawbacks faced by conventional Pt/C catalysts. However, their application in practical fuel cell electrodes still faces big challenge due to their unusual morphology and bulky volume. This review focuses on the recent progress from 2010 in 1D electrocatalysts for oxygen reduction reaction (ORR) and hydrocarbon (methanol, ethanol and formic acid) oxidation reaction in PEMFCs, covering Pt-based and non-Pt precious metal nanostructures, as well as non-precious metal catalysts (NPMCs). The correlations between the morphology, composition and catalytic properties of these catalysts are discussed. Critical perspectives are devoted to the increasing gap between the pure materials research and the fuel cell development in this emerging research area (222 references).

Keywords: Nanowire; nanotube; electrode; direct methanol fuel cell (DMFC); direct formic acid fuel cell (DFAFC)

1. Introduction

The growing pressures from energy demand and environmental pollution have motivated search for alternative clean and sustainable power generation technologies. The fuel cell, which can directly convert chemical energy (e.g. H_2) into electrical power at high energy efficiency with low carbon and NO_x emission, is one of the promising candidates for the replacement of conventional combustion-based power generators [1]. Of the multitude of fuel cell technologies available, polymer electrolyte membrane fuel cells (PEMFCs) have been receiving extensive attention, due to their low operational temperature, easy start-up and shutdown and flexible power ranges in applications [2]. Despite the initial demonstrated application of PEMFCs, the large-scale commercialization has been remarkably hindered by several technological challenges, in particular the low catalytic activity, high cost, poor durability and reliability of fuel cell electrodes. In PEMFCs, the power generated is from two electrochemical reactions, namely fuel (e.g. hydrogen or hydrocarbons) oxidation reaction at anode and oxygen reduction reaction (ORR) at cathode [3]. Electrocatalysts are required to promote the on-going of the electrochemical reactions and Pt is still considered as one of the best electrocatalysts for PEMFCs up to today [4]. Besides the high cost of catalysts, the slow electrode kinetics and irreversible CO poisoning greatly influence catalyst activities in electrodes, and the harsh operational conditions also cause durability issues for a long-term operation [5]. All of these challenges drive researchers to develop highly economical, active and robust electrocatalysts to make PEMFCs commercially successful.

The commonly used strategies to reduce the loading amount of Pt in PEMFCs while guaranteeing the performance level include dispersing Pt nanoparticles (NPs) on high surface area carbon support, optimizing catalyst size, shape, structure and morphology, as well as incorporating other transition metals to form Pt alloy or hybrid nanostructures. Shao et al. [6]

showed that the ORR specific activity of Pt improved rapidly with the increased particle size from 1.3 nm, and the mass activity reached the maximum value at 2.2 nm. Pt NPs with various shapes [7] (e.g. cubic, tetrahedral, truncated octahedral and high-index tetra-hexahedrons) and different structures (e.g. solid, hollow and porous) have been synthesized and demonstrated. Multi-component NPs such as core-shell [8, 9] and alloy NPs [10, 11] have also been prepared and enhanced catalytic activities observed. Although excellent catalytic activities are achieved with these NPs, the small size of these spherical nanoparticles usually induces severe degradation during PEMFCs operation. The high surface energy of zero-dimensional (0D) structural feature renders small particles more susceptible to dissolution, which is more pronounced in the crucial cathodic environment in practical PEMFCs. The dissolved particles will redeposit on larger ones, making larger particles even large and smaller ones even small, which is defined as the Ostwald ripening process. In order to reduce the surface energy, another reshaping process named agglomeration also occurs when these smaller NPs come in contact each other. Moreover, the corrosion of carbon support materials also contributes to the catalyst degradation, leading to detachment of catalyst NPs from the support and sintering on the membrane, resulting in poor fuel cell performance [12, 13]. To address these issues, novel nanostructures with excellent stability are urgently required for practical applications.

2. Advantages of 1D nanostructures for PEMFC applications

One-dimensional (1D) nanostructures, such as nanorod (NR), nanowire (NW), nanotube (NT) and nanochain (NC) represent a promising morphology paradigm that may overcome some inherent drawbacks of 0D NPs. 1D motifs, in particular single-crystal nanostructures, allow for the preferential exposure of low energy crystal facets and lattice planes with fewer lattice boundaries [14, 15]. The displayed facets would help reduce the surface energy of the whole

system and be highly active for the catalysis. The smooth single-crystalline planes can also minimise the number of undesirable low-coordination defect sites which are less catalytically active and vulnerable to oxidation and decomposition. Besides, 1D nanostructures can facilitate the electron transport by the path directing effects in catalyst electrodes and thus enhancing the reaction kinetics on the catalyst surface [16]. Furthermore, it has also been predicted that when the diameter of 1D nanostructures decreases below a critical value of 2 nm, their electrocatalytic activity will be improved due to a surface contraction effect [17].

In terms of the catalytic stability, due to their asymmetric structure, 1D nanostructures are able to alleviate the dissolution, aggregation and Oswald ripening that the NPs usually suffer from [18]. Benefitting from the relative large scale length and the retained electrical conductivity as compared with NPs, 1D nanostructures are less inclined to require a carbon support for dispersing NPs and conducting electrons, thus can potentially address the support corrosion problem faced by commonly employed Pt/C catalysts [19].

All of these noteworthy advantages of 1D nanostructures provide the potential to reduce the precious metal loading without compromising the electrocatalytic activity but with a better durability. In light of these, 1D nanostructures, as a new direction for superior electrocatalysts in PEMFC applications, have attracted considerable efforts.

3. Preparation of 1D Catalysts for PEMFC applications

Recent developments in material synthesis methods have enabled the fabrication of many novel 1D nanostructures with precisely controlled shape, composition and structure, bringing in a step forward to the fuel cell research and development.

The earliest approach explored for the synthesis of Pt-based nanowires as fuel cell catalysts is template preparation method, which starts from the use of mesoporous silica SBA-15 to produce a nanowire network [20]. The diameter and length of the prepared

catalysts can be adjusted by controlling the pore diameter and length of templates. This straightforward route has been actively explored and a range of templates such as mesoporous silica [21], anodic aluminum oxide (AAO) [22], ZnO [23], etc. have been applied. Considering the complicated process of template removal, contrary to these hard templates, some soft templates including polymers [24] and viruses [25] have also been used to generate 1D morphology.

Apart from the template method, an electrospinning technique has also been employed to prepare 1D catalysts. With the ability to control the porosity, the fibre diameter and length, the produced 1D nanomaterials exhibit good catalytic performance [26]. However, in order to well disperse the inorganic precursors, surfactants are usually added and needed to be removed in the post-treatment process. The remaining surfactants may cover the catalyst surface, resulting in a low catalytic performance [27].

Although the template and electrospinning techniques could benefit for the production of 1D morphologies, both of them require to remove either templates or surfactants to obtain pure products. Moreover, only polycrystalline nanostructures could be obtained during the synthesis process, which limits the further performance improvement [28]. Compared with polycrystalline 1D nanostructures, single-crystalline counterparts possess longer segments of smooth crystal planes, fewer lattice boundaries and a lower number of surface defect sites, which are confirmed to be beneficial for the electrocatalytic reactions [29]. The wet-chemical routes containing both organic solvent and aqueous solution approaches have been then demonstrated to successfully synthesise single-crystalline 1D nanostructures for fuel cell catalysts.

In 2004, Xia et al. [30] for the first time demonstrated that the reaction rate is a good control tool for producing 1D Pt nanostructures. They prepared single-crystal Pt nanowires through a polyol process at 110 ^{o}C combined with poly(vinyl pyrrolidone) (PVP) as

surfactant and a trace amount of iron species to further slow the reaction rate. After that Bi^{3+} was also introduced to decrease the reaction growth rate to form Pt-Bi nanowires [31]. However, similar to the electrospinning method, the polyol process also has the problem of removing surfactants. To address this problem, the oleylamine method, without using surfactants or ligands, was adopted to synthesize Pt-Fe nanowires [32]. Nevertheless, the high reaction temperature and the requirement of protective gas flow also limit the use of this method. Hence, there is a continuous need for the development of facile synthesis techniques which are environmental friendly, surfactant-free, cost-effective, etc. to obtain high-quality single crystalline 1D catalysts. In 2007, Sun et al. [33] successfully developed an efficient aqueous approach for the large-scale synthesis of single crystal Pt NWs by using formic acid as the reducing agent. This method is much simpler than the above-mentioned approaches because it doesn't need any templates, surfactants, organic solvents, capping agents or induced growth catalysts and can be directly performed at room temperature with mild formic acid as reductant, which makes it a promising method for the synthesis of 1D Pt nanostructures for fuel cell catalysts. Based on this method, they prepared self-assembled three-dimensional (3D) Pt nanoflowers (NFs) [34], multiarmed starlike Pt NWs [35], and 3D hybrid nanostructures with Pt NWs on Sn@CNT nanocable [36]. The single crystal effect with 1D morphology of these 1D Pt nanostructures brought in excellent catalytic activity and durability towards ORR.

Very recently, based on the improved understanding of the crystal nucleation and growth mechanisms, a few other methods have been developed to generate 1D structural motifs in aqueous solvents, including electrochemical deposition [37], galvanic replacement [38], thermal decomposition [39], seed mediated growth [40], organic-sol [41, 42], hydrothermal synthesis [43], and a combination thereof.

However, there're still big challenges faced by 1D nanostructures for their real applications in fuel cells. These include the unusual morphology and the bulky volume of 1D nanostructures as compared to conventional Pt/C nanoparticles. The unusual morphology brings big difficulties for 1D nanostructures in fabricating fuel cell electrodes by approaches used for conventional Pt/C electrodes, and the bulky volume results in smaller specific surface areas thus a lower mass activity. These challenges were previously summarized by Du in his review paper [28]. In this review, considering the progresses in addressing these challenges, we focus on the very latest efforts on 1D electrocatalysts in recent five years, concentrating on the rational synthesis of precious metal based elements, alloys, and hybrid structures, as well as non-precious metal catalysts (NPMCs) for two crucial electrochemical reactions in PEMFCs. The correlation between the electrocatalyst structure and electrocatalytic performance is further discussed. Considering the requirements for practical PEMFC electrodes rather than just pure catalyst research, the challenges facing the development of 1D nanostructures and the prospect to replace the current commercial Pt NP catalysts for PEMFC applications are explored. An overview of all references cited including the 1D nanostructures, the preparation approaches and the achieved results is listed in Table 1 at the end of this review.

4. 1D nanostructured catalysts for oxygen reduction reaction (ORR)

Since the kinetics of ORR is ca. 6 orders of magnitudes slower at cathode than the hydrogen oxidation reaction (HOR) at anode, the performance of a hydrogen-air fed PEMFC mainly limits by this sluggish reaction. Many studies have been conducted to find catalytic mechanisms of the multi-electron ORR, which could be helpful for the design of better catalysts to drive this rate-limiting reaction. However, the understanding of the ORR mechanism is not easy owing to the challenges of intermediates in-situ identification, kinetic

data unambiguous interpretation as well as electronic structure explicit calculation [44]. Although the detailed process of this complex multistep reaction is still under debate today, the commonly accepted ORR mechanism in acid solution involves O_2 adsorption, proton and electron transfer step, followed by the O-O bond breaking [45]. It is believed that the binding energies of reactive intermediates such as oxygenated (O*), hydroxyl (OH*) and superhydroxyl (OOH*) species determine the overall ORR process [46, 47]. For catalysts that bind these species too weakly, the rate is limited by proton and electron transfer to dissociate O_2 while for catalysts that bind these intermediates very strongly, the rate is limited by reaction products to desorb from the surface [48]. Therefore, the optimal catalytic activity can be achieved with "moderate" binding energies of these reactive intermediates on catalyst surface. In consideration of this, the oxygen adsorption energy (ΔE_O) is considered as a good descriptor for the catalytic activity. A volcano plot (Fig. 1a) has been developed by Nørskov et al. [49] to describe the relationship between ORR activity and ΔE_O. The metals located on the left side of the volcano peak bind oxygen too strongly while the right side of the metals have a weak oxygen binding ability. Among the pure metals, Pt is the most active one and it locates closest to the volcano peak. Besides of pure metals, Pt-based transition metal alloys can possibly provide further enhanced activities, and the trend was explained by Greely et al. [45] with another volcano plot (Fig. 1b). It demonstrates that a surface that binds oxygen 0.0–0.4 eV more weakly than Pt (111) will be better, with 0.2 eV weaker than that of Pt as the optimum situation. Therefore, many efforts have been made to develop catalysts with ΔE_O around 0.2 eV positive than that of Pt to improve the ORR kinetics [48].

(Fig. 1 here)

Another descriptor to indicate the adsorption energy of adsorbates on metal surfaces is the d-band centre (ε_d) model which illustrates the position of ε_d relative to the Fermi Level (ε_F) [50]. Unlike the difficult measurement of ΔE_O, ε_d is experimentally accessible and regarded

as the simplest descriptor with good accuracy. The shift of ε_d results from the variation of electronic structure which is further controlled by the filling state of electrons. Taking oxygen atom adsorption on the Pt surface as an example, the coupling of O 2p state with Pt d electrons causes oxygen resonance to split into two states: a fully filled bonding state below ε_F and a partially filled antibonding state across ε_F. A downward shift of ε_d to ε_F will lead to more filling of antibonding states and thus to a weaker bond, which is favorable to ORR [51]. Hence, the d-band centre is regarded as the ultimate indicator to predict the catalytic activity for ORR. The understandings provide the basis for the design of novel 1D nanostructured materials to catalyse ORR.

4.1 1D Pt-based catalysts for ORR

On account of the outstanding catalytic and electrical properties, coupled with the excellent corrosion resistance, Pt-based catalysts are still the most efficient electrocatalysts for ORR, especially in acidic medium as they can effectively impede the formation of adsorbed oxygenated intermediates at potentials above 0.8 V and improve ORR kinetics via lower energy pathways [52]. Therefore, to overcome the drawbacks of low intrinsic activity and poor stability of conventional Pt NPs, some work has been conducted on the combination of the respective advantages of Pt and 1D nanostructures to design novel 1D Pt-based catalysts. Many exciting achievements have been reported in recent years, including pure Pt, Pt-based alloy and Pt-based hybrid catalysts.

4.1.1 1D Pt nanostructured catalysts for ORR

To further understand the catalytic mechanism of 1D nanostructures, electrodes which are made up of only one Pt nanowire were fabricated separately by two groups of Li [53] and Percival [54] to explore the competition effect of neighbouring catalyst particles for reactants

on the ORR kinetics. They got a similar conclusion that the radius of nanowire affected the electrocatalytic activity, although it was also observed that the tip end position was more active than the sidewall position. The observations can help understand the structure-function relationship in single nanowire level and provide implications for the synthesis and selection of novel catalysts with high efficiency. However, the two reported work only covered the Pt NWs down to 4 nm. For a much thinner 1D nanostructures with a higher surface to volume ratio, e.g. 2–3 nm, with which a much enhanced catalytic activity was usually achieved, a further study is required.

Ultrathin Pt nanowires

Ultrathin 1D nanostructures have been explored to increase the surface-area-to-volume ratio for a large electrochemical surface area (ECSA) and thus an enhanced catalytic activity. Unlike either the extremely small nanoparticles or the large bulky volume of Pt NWs, these ultrathin 1D nanostructures don't suffer from the physical ripening and aggregation process or have a mass transport limitation in practical application. Assisted by chromium hexacarbonyl [$Cr(CO)_6$], Xiao et al. [55] synthesized Pt ultrathin NWs with a uniform diameter of 2–3 nm by a pyrolysis approach in oleylamine. The length can reach up to several microns. The mass activity of Pt NWs (88 mA mg^{-1}) is comparable to that of Pt/C (85 mA mg^{-1}, 45 wt% Pt on Vulcan XC-72 carbon support, Tanaka). Ruan et al. [56] developed ultrathin multiple-twinned Pt NWs with a diameter of about 2 nm and a high density of twin planes by biomimetic synthesis using a specific Pt-binding peptide (amino acid sequence Ac-TLHVSSY-CONH2, named BP7A, identified through phage display). The material achieved a mass activity of 144 mA mg^{-1}, a 58.2% increase compared with the Johnson Matthey (JM) Pt/C catalyst (20 wt% Pt on Vulcan XC72R carbon support). After a 6000-cycle accelerated degradation test (ADT), they only showed a loss of 14.2% of their initial ECSA, comparing

with a severe degradation of 56.7 % of JM Pt/C catalyst. Koenigsmann et al. [17] synthesized even thinner Pt NWs with a diameter of 1.3 nm through the reduction of H_2PtCl_6 by $NaBH_4$ in the mixture of N,N-dimethyl formamide (DMF) and toluene, followed by a treatment with an acid wash protocol. The as-prepared Pt NWs displayed an outstanding high specific activity of 1.45 mA cm^{-2}, which was nearly 4 times greater than that of analogous, unsupported platinum NTs and 7 times greater than that of Pt/C NPs (Fig. 2). It is confirmed that the acid washing exfoliates the nanowires and re-dissolve amorphous platinum deposits so as to expose the active surface areas of the wires themselves, and this is also confirmed working for the conventional Pt NPs.

(Fig. 2 here)

Pt nanotubes

Another common 1D Pt nanostructure is Pt NTs, which normally show higher specific surface areas than the same size Pt NWs. Pt NTs are usually prepared by either the template synthesis method (i.e. with anodic aluminum oxide template (AAO)) or the galvanic replacement reaction (i.e. from Ag or Cu nanowires). Un-supported Pt NTs could be easily synthesized by the decomposition of a platinum acetylacetonate vapour within anodic alumina (AAO) templates [57]. In this case, the nanotubes obtained are usually large nanoparticulate aggregates composed of small Pt crystallites. Although a higher specific activity can be achieved, the mass activity is usually much lower than Pt/C. In terms of this, the galvanic replacement approach can partially address this drawback. For example, porous polycrystalline Pt NTs [13] with a wall thickness of 5 nm, an outer diameter of 60 nm, and a length of 5–20 μm were synthesised through galvanic displacement from Ag nanowires and showed a slightly higher mass activity than Pt/C (Pt NT: 88 mA mg^{-1}; Pt/C: 84 mA mg^{-1}). A post hydrothermal treatment can evolve the polycrystalline Pt NTs to single crystalline Pt

NTs [58], which can further improve the catalytic activity and stability. Single crystal porous Pt dendritic NTs were also reported with Ag dendrites as templates [59]. The unique structure with characteristics of porous, hollow, hierarchical, and single crystallite not only renders a large surface area with a high catalyst utilization, but also improves mass transport and gas diffusion. These novel Pt structures exhibited a significantly improved catalytic activity (4.4 fold) for ORR and greatly enhanced durability (6.1 fold) over the state-of-the-art Pt/C catalyst (E-TEK, 30 wt% Pt/Vulcan XC-72). Instead of using Ag nanowires, more cost-effective Cu nanowire templates have also been employed to prepare Pt NTs [60].

Other 1D nanostructures

Other 1D nanostructures were also investigated for ORR. For example, vertically-aligned Pt NRs were fabricated on glassy carbon electrodes through the glancing angle deposition (GLAD) technique [61]. The length of nanorods varied between 50 and 400 nm, but only a large diameter was achieved, which could be up to 100 nm, resulting in a lower mass activity. Pt nanochains (Pt NCs) were synthesized by a one-pot hydrothermal decomposition method through oriented attachment of spherical Pt nanoparticles [62]. The obtained NCs with a diameter of 5–10 nm interconnected with each other and acted as building blocks to form a network structure, exhibiting a similar mass activity to the commercial E-TEK Pt black. Fu's group [63] prepared polyallylamine (PAH) functionalized single crystal Pt nanolances (Pt NLs) through a hydrothermal reduction route in a two-phase water-complex system. 1D Pt NLs were formed due to the strong Pt-N bond interaction between Pt nucleation and PAH. The diameter of the NLs was about 5–15 nm and the length was about 50–200 nm. Although with a smaller ECSA, Pt NLs still showed a comparable ORR activity and a better durability than that of Pt black (JM).

Supported 1D Pt nanostructures

The reported synergistic effect between Pt catalysts and supports [64] indicates that the ORR catalytic activity can be further improved by synthesizing supported 1D Pt nanostructures. The electron donation from the support to Pt leads to a decrease in the Pt d-band vacancy and thus outstanding ORR activities. Shimizu et al. [65] synthesized Pt NWs via spray drying and hydrogen reduction, using SiO_2 NPs as spacers. After 27,000 redox cycles, benefiting from the excellent chemical stability of SiO_2, the catalysts still retained 77% of their initial activity. Through formic acid reduction method, Pt nanodendrites (Pt NDs) anchored on bamboo-shaped carbon nanofiber arrays (CNFAs) [66] and Pt NWs grown on $Ti_{0.7}Ru_{0.3}O_2$ were fabricated [67]. For Pt NDs/CNFAs, the uniform dispersion of Pt NDs and improved catalyst-support binding could contribute to the improved ORR activity. Regarding PtNW/$Ti_{0.7}Ru_{0.3}O_2$ catalysts, the multifunctional $Ti_{0.7}Ru_{0.3}O_2$ not only plays an important role as support but also as co-catalyst to catalyse ORR.

As a class of two-dimensional carbon material, graphene has many advantages such as high electrical conductivity, huge surface area, unique electronic properties and high thermal and chemical stability, owing to the graphitized basal plane structure. Graphene-supported metal nanostructures have emerged as a new class of catalysts due to the metal-support interactions and improved conductivity of the catalysts. Most of them were synthesized via aqueous reduction process, using either $NaBH_4$ or formic acid as reductant to synchronously reduce the Pt precursor and graphene oxide in one pot. Branched Pt nanostructure on graphene were produced via $NaBH_4$ reduction process [68]. The electrons involved in ORR is around 3.4–3.7, nearly matching the theoretical value of 4. Pt NWs grown on sulfur doped graphene (SG) were prepared by using formic acid as reductant and showed enhanced catalytic activity towards ORR [69]. Compared with pristine graphene support, sulfur doped graphene (SG) seems to provide higher density of anchoring sites,

which is favourable for Pt nucleation under lower reactant concentrations. The strong metal-support interactions between Pt and SG result in uniform distributed Pt NWs on support surface, as shown in Fig. 3. Another excellent approach is to modify the graphene surface for a better contact with 1D Pt nanostructures. For example, Pt NDs supported on genomic-double-stranded-DNA (gdsDNA) modified reduced-graphene-oxide (rGO) was reported showing a much higher ORR activity [70]. The mass activity and specific activity obtained during rotating disk electrode (RDE) measurement at 80 °C is 1.01 A mg^{-1} and 1.503 mA cm^{-2}, which is 5.5 and 1.7 times higher than that of Pt/rGO, respectively. Moreover, after 10,000 cycles for the ADT, the half wave potential in ORR polarization curves almost showed no change. The authors attributed the excellent ORR performance to the introduction of gdsDNA, which interacted with rGO sheets through π-π interactions and resulted in good conductivity of the catalysts.

(Fig. 3 here)

4.1.2 1D Pt-based alloy catalysts for ORR

To reduce the loading of expensive Pt while increasing the ORR activity, another very effective strategy is to introduce non-Pt or even non-precious metals into the Pt catalysts to form bi- or multi- metallic alloy catalysts. Compared with Pt, density functional theory (DFT) demonstrated that alloying Pt with other metallic elements can lead to the change of Pt-Pt interatomic distance, a downshift of the d-band centre, and the increase of d-band vacancy, leading to a more favourable adsorption of oxygen intermediates [71], allowing the individual element to work synergistically and improving the catalytic performance [72]. 1D Pt-based alloy catalysts, combining both advantages of Pt multimetallic features and the 1D morphology, can mutually and synergistically accelerate the ORR rate.

1D Pt-based precious bimetallic nanostructures

Various precious metals such as Pd, Ag and Au have been introduced in Pt to form alloy catalysts with different morphologies. Among these three precious metals, Pd is a promising candidate as it has a similar valence shell electronic configuration and lattice constant to Pt [73]. The lattice mismatch between Pt and Pd is only 0.77%, which endows PtPd alloy similar properties to pure Pt. Additionally, compared to Pt, the cost of Pd is slightly lower and the availability on earth is two hundred times higher [74]. Therefore, it is a good choice to add Pd into Pt to design better ORR catalysts.

By using Te nanowires as templates, PdPt alloy NWs were prepared in wet chemical solution [75]. The NWs had an average diameter of about 10 nm and length up to tens of micrometres. The RDE testing showed more than double mass activities over the commercial 20% Pt/C. Starting from Pd nanowires, PtPd porous nanorods (PNR) were synthesized through a bromide-induced galvanic replacement reaction [76]. PtPd PNRs had an average diameter of 35 nm and a length up to 2 μm. The porous structure led to more than 3 times higher ECSA and 40% higher specific activity than Pt/C (40 wt%, from Alfa Aesar). This structure also exhibited an excellent durability with only 5.88% loss of the initial ECSA after the 1000 potential cycles of ADT in alkaline solution, as compared to 40.4% loss of the commercial Pt/C catalyst. Wang's group [77-80] prepared carbon supported PtM (M=Au, Pd, Ag) NRs by a formic acid reduction method and studied their ORR activity and stability by both of electrochemical measurement and DFT calculations. The results demonstrated the ORR enhancement stemming from the high aspect ratio and alloying, which lessened the effect of dissolution, aggregation and Ostwald ripening, and also led to a weaker Pt-O^- binding.

1D Pt-transitional bimetallic nanostructures

Previous computational and experimental studies pointed out that Pt alloyed with a transition 3d metal such as Fe, Co, Ni and Cu could show dramatic performance enhancement in ORR catalysis [11, 45, 81]. The transition metals could decrease the absorbed OH species on the active Pt sites and at the same time Pt can provide kinetic stability against the dissolution of the non-precious component, resulting in an improved ORR activity and stability.

Nanoporous PtFe alloy NWs [82] with a diameter of 10–20 nm were synthesised by electrospinning and chemical dealloying techniques. The porous long nanowires interweaved to form a self-supporting network, showing 2.3 times specific activity (0.38 mA cm^{-2}) to Pt/C catalysts (0.19 mA cm^{-2}_{Pt}, 40% Pt/C, E-TEK). After 13,500 potential cycles, only 4% mass activity was lost versus the 38% loss of that of Pt/C. Ultrathin PtFe alloy NWs with diameters of 2–3 nm were prepared through an organic solution reduction method using oleylamine [83]. The obtained catalysts demonstrated two times better mass activity and durability than Pt/C. Sun's group [84] synthesized thin PtFe and PtCo NWs with an average diameter of 2.5 nm via a similar organic-phase decomposition and reduction process. The as-prepared NWs deposited on carbon support (Ketjen EC-300J) and then washed with acetic acid to remove the surfactant and part of Fe or Co. The experimental results showed that the composition-dependent ORR activity could not be well represented by the PtFe and PtCo NWs owing to the loss of Fe and Co during the acetic acid treatment. The surface specific and mass activities of PtFe NWs reached 1.53 mA cm^{-2} and 844 mA mg_{Pt}^{-1}, respectively. If an annealing treatment was introduced, a Pt skin could be formed on the surface of nanowires, enhancing the ORR activity and stability. The annealed 6.3 nm PtFe NWs showed an even higher specific activity of 3.9 mA cm^{-2}. Combining post-synthesis annealing and electrochemical dealloying, PtCu alloy on Cu nanowire surface (PtCu/CuNW) was achieved [85]. The compressive strain and low Pt content both contributed to high specific and mass activities, which are 2.65 mA cm_{Pt}^{-2} and 1.24 A mg_{Pt}^{-1}, respectively. Recently, vertically

aligned PtNi alloy nanorod arrays were synthesized through a magnetron sputtering GLAD technique and exhibited a superior mass activity which is 2.3–2.5 folds higher than that of pure Pt nanorods [86]. But the nanorods were also observed to lose activity during potential cycling concomitant with the loss of Ni in spite that a much improved stability was obtained as compared to Pt nanorods and Pt/C.

Since Xia's group [87] reported the preparation of precious metal (Pt, Pd, Au) nanotubes through a galvanic displacement reaction by using Cu nanowires as sacrificial templates, the synthesis of tubular electrocatalysts has received increasing interest, especially the bimetallic PtCu alloy NTs [88, 89]. In the reaction, Cu nanowires were partially replaced by Pt, followed by an acid treatment to remove some Cu, then NTs consist of PtCu alloy would be formed. Cu NWs here not only functioned as templates but also provided alloying of the remaining Cu atoms with Pt. Cui et al. [90] also prepared PtCu tubular catalysts with an AAO template. Thermal annealing was then introduced to increase the surface Pt atomic fraction and lattice ordering, and a potential cycling treatment in acidic electrolyte was used to partially dissolve Cu atoms to obtain a high ECSA. This adsorbate-induced morphology restructuring process finally rebuilt a highly rough surface, displaying an enhanced specific and mass activity of 0.8 mA cm^{-2} and 232 mA mg^{-1}, respectively. The TEM images and surface evolution schematic are shown in Fig. 4.

(Fig. 4 here)

1D Pt-based multimetallic alloy nanostructures

Going a step further from bimetallic alloy nanomaterials, multimetallic alloys have been the subject of intensive studies. The multicomponent nature with multimetallic alloys means different elements could work synergistically at a possibly higher efficiency than bimetallic alloys. Ternary PtNiFe NWs [91], PtFeM (M=Cu, Ni) [92] and PtNiCu [93] NRs have been

synthesized in organic phase for the ORR application. The results showed that they generally possessed higher mass and specific activities than the binary alloys. Using Cu nanowires as sacrificial templates, Yu's group [94] synthesized PtPdCu nanoparticle nanotubes by galvanic displacement with partially sacrificial Cu nanowire templates, and followed by the electrochemical leaching of the non-noble metal Cu in the acidic electrolyte. Quaternary PtCuCoNi alloy NTs with an ultralow content of Pt have also been synthesized by an AAO template-assisted electrodeposition approach [95]. The multicomponent nature coupled with hollow configuration of NTs enabled an improved ORR activity, showing a mass activity 17.5 and 5.0 times higher than that of Pt black (BASF) and Pt/C catalysts (30 wt% Pt, BASF), respectively.

4.1.3 1D Pt-based hybrid catalysts for ORR

Besides alloys, another efficient way to reduce the content of Pt is to develop Pt-based hybrid catalysts. Unlike alloy nanomaterials which usually have a homogeneous element distribution, hybrid nanomaterials with core-shell structure or heterostructure architectures have a heterogeneous atomic arrangement [96]. In this case, the precious metal shell can partially address the leaching problem of transition metals as that in alloyed nanostructures under the crucial fuel cell operating conditions, thus slowing the degradation rate of catalysts [97]. Besides, they often offer a variety of parameters such as the composition of the core, the thickness of the shell, the structural morphology etc., which collectively control the catalytic properties [9]. Similar to alloyed catalysts, Pt-based 1D hybrid catalysts not only minimize the Pt usage but also offer desired interactions to tune both electronic and surface strain effects, facilitating electron conduction and the stabilization during the catalysis process as well [72].

1D Pt-based core-shell structure

The unique structure of core-shell architectures captures growing interest in the research community. Pt-based core-shell catalysts are characterised by a thin Pt shell on proper metal cores. In general, the formation involves the generation of an interior core and a further growth of an exterior Pt shell on all faces of the core. The commonly used methods for the controlled synthesis of core-shell structure include the underpotential deposition (UPD) replacement, the structural rearrangement (dealloying or segregation) and the seed-mediated process [98]. By partially galvanic displacing Cu NWs, Pt with a layer thickness of 2 nm coated on Cu NWs were obtained, and the specific ORR area activity could reach 1.50 mA cm_{Pt}^{-2} [60]. An alternative catalyst system to transitional metal cores is to include non-Pt precious metal cores, such as Pd or Au in 1D structures for a long-term stability in acidic media. Koenigsmann et al. [99] synthesized carbon supported ultrathin Pd-Pt core-shell NWs by using 2 nm Pd NWs as core and achieved Pt monolayer shell through Cu UPD displacement. In this work, it was also found that a post UV-generated ozone treatment endowed NWs with the retention of morphology and dispersion on carbon support, enhancing the specific activity and durability by 1.5 and 1.4 folds, respectively. The obtained catalysts displayed outstanding mass and specific activity of 1.83 A mg^{-1} and 0.77 mA cm^{-2}, respectively. After 20,000 cycles, the NWs still maintained 71% of their initial ECSA. Considering the enhancement effect that has also been achieved for other nanostructures with UV treatment [100], this post modification approach can possibly find a high potential in PEMFC catalyst development after a further understanding of the detailed mechanism. Through a similar Cu UPD approach, Pd-Pt core-shell NWs supported on multiwalled carbon nanotubes (MWCNTs) were synthesized [101]. With direct partial galvanic displacement of Pd NTs, Alia et al. synthesized Pd-Pt core-shell NTs [102] with a wall thickness of 6 nm. Without exploiting electrochemical procedures or contaminating mediators such as Cu, Pd-Pt

core-shell NWs were also prepared in aqueous solution by a hydrogen sacrificial protective method [103].

Core-shell structures with extended bi- or multi- metallic core or shell have also been reported. Through UPD followed by galvanic replacement with Pt, ultrathin nanowires (~2 nm) with PtAu binary shell and Pd core were synthesized and the structure-property correlations were investigated [104]. Combining the experimental results and DFT calculations, it is revealed that Au atoms underwent surface segregation and a restructuring happened during the galvanic replacement process. By kinetically controlling the nucleation and growth process, Pt-Au core-shell NRs with PtAu shell were prepared through a formic acid reduction process [105]. Treating FePtM (M=Cu, Ni) NRs with acetic acid and by electrochemical etching, Sun's group [92] converted the ternary alloy NRs into core-shell FePtM/Pt NRs. Recently, this group reported the further synthesis of FePtM/FePt (M=Pd, Au) NWs through a seed-mediated method [106]. The FePt shell with an optimal thickness of 0.8 nm exhibited a mass and specific activity of 1.68 A mg^{-1} and 3.47 mA cm^{-2}, respectively. Based on the outstanding ORR activity of Pt_3Ni, self-supported core-shell Au/Pt_3Ni NWs consisting of small-sized Pt_3Ni nanodendrites on Au nanowires were synthesized in organic phase by using oleylamine [107]. Compared with Au/Pt core-shell structure, Au/Pt_3Ni displayed more than twice ORR activity and durability.

1D Pt-based heterostructure

In addition to the core-shell structures, heterostructures offers an alternative hybrid catalyst model for the ORR and fuel cell applications. It can partially benefit from the synergistic effect of different metal compositions for accelerated ORR kinetics and at the same time be fabricated through an easier method compared with the core-shell approach. Xia's group [108] synthesized Pd-Pt bimetallic NDs through a seed-mediated approach and investigated

nucleation and growth mechanisms involved in the synthesis. Fig. 5 shows the growing process of Pt on Pd nanoseed surface. According to their study, Pd seed played a crucial role in the formation of open, dendritic structure. Otherwise, only foam-like Pt aggregates formed under identical conditions. This dendritic nanostructure could also be supported on MWCNTs to provide even higher activities [109]. By introducing metal Bi in the synthesis process, Pt-on-$Pd_{0.85}Bi_{0.15}$ NWs with a diameter of 8.3 nm and length of 387 nm were synthesized in an oil phase [110]. Benefiting from the synergistic effect of trimetallic composition and the favouring electron transmission by 1D nanowire structure, the as-prepared catalysts showed superior electrochemical performance with a mass and specific activity of 1.16 A mg^{-1} and 1.48 mA cm^{-2}, respectively.

(Fig. 5 here)

4.2 1D non-Pt based catalysts for ORR

Although Pt-based nanostructures are still the most frequently used catalysts for ORR, the high cost and limited supply can hardly meet the demands for widespread applications of PEMFCs. From a long-term point of view, exploring and synthesizing non-Pt based catalysts seems to be an emphasis for future research. Due to the unique properties of the 1D morphology, great efforts have also been made to find 1D Pt alternative catalysts for ORR. Recent developments in this field reveal that the relatively cheap and abundant precious metals (Pd, Au and Ag) and their multimetallic alloys, transition metal chalcogenides, metal oxide based nanocrystals and N-doped carbon nanotubes can be potential substitutes for Pt-based electrocatalysts towards ORR, especially in alkaline media.

4.2.1 1D non-Pt precious metal group catalysts

1D non-Pt precious metal group catalysts, including Pd, Au, Ag and their alloys have all been reported in recent years, but mainly for ORR in alkaline media. 45 nm Pd NWs [111] were synthesized based on polycarbonate template method under ambient surfactantless condition and compared with 2.2 nm ultrathin Pd NWs obtained by a wet-chemical technique with surfactant [112] to investigate the size-dependent ORR behaviour. The results revealed a distinctive size-dependent electrocatalytic enhancement of nearly 2-fold with the decrease in wire diameter. By galvanic displacement of Ag NWs, Pd NTs with a wall thickness of 6 nm were synthesized [113], which could produce 3.7 times greater ORR activity than Pt/C. CuPd bimetallic NWs with an average width of 18.2 nm were prepared by colloidal method [114]. Investigation of the growth process revealed that the nanowires were formed by attachment of spherical particles and strongly influenced by interactions between surface ligands (PVP) and metals. The obtained catalysts showed comparable ORR activity to Pt in acid media. PdFe nanoleaves with Pd-rich nanowire "veins" and Fe-rich "blades" were synthesized through a wet-chemical route [115]. The ultrathin Pd NWs with a very small diameter of 1.8–2.3 nm enhanced the surface oxidation resistance. The unique high surface area and nanoleave structure together contribute to the ORR performance with a specific activity of 0.312 mA cm^{-2} and a mass activity of 159 mA mg^{-1} in NaOH electrolyte. Core-shell Pd-coated β-MnO_2 nanorods [116] were also synthesized via electroless deposition method.

Au is another precious metal which has been extensively studied as electrocatalysts for ORR. Au NDs supported on reduced graphene oxide [117] prepared in aqueous solution have been demonstrated competitive activity and better stability toward ORR in alkaline medium as compared to Pt/C catalysts. Wong's group [118, 119] compared PdAu NWs synthesized by wet-chemical and template-based methods to investigate the size and composition dependent enhancement of ORR performance. The experimental results demonstrated a similar specific activity of 2 nm PdAu NWs prepared via the wet-chemical

method and that of the 50 nm ones obtained by the template-based method. Similar to the preparation of Pd NTs by galvanic displacement of Ag NWs, Au NTs with a wall thickness of 6 nm were synthesized [113], exhibiting even 2 times greater ORR activity than Pt/C. By using a two-step galvanic replacement reaction technique, porous Pd shell coated Au nanochain networks [120] were fabricated and achieved better activity and higher stability in alkaline solution, which is presumably due to the porous Pd shell and nanochain Au core. Recently another core-shell structure Au@Pd nanothorns were prepared for the first time through a co-chemical reduction method [121]. The diameter of the as-prepared nanothorn head is around 30–50 nm and the length is about 100–400 nm. Owing to the unique porous structure and the synergistic effect between the Pd shell and Au core, the obtained catalysts exhibited a higher ORR activity and stability in alkaline solution comparing to the commercial Pd and Pt black.

As one of the important precious metals, Ag is much cheaper than Au and Pd. Due to the simple preparation approach, 1D Ag nanostructures are commonly employed as a sacrificial template for synthesizing electrocatalysts. Recently, nanostructured Ag is also used directly in alkaline medium to catalyse ORR. Versatile 1D Ag@POA (poly(o-anisidine)) core-shell nanostructures such as nanobelts, nanowires and nanocables were fabricated by rational adjustment of the preparation conditions [122]. Through polyol process or hydrothermal method, Ag nanorods [123] and Ag nanowires supported on MWCNT-incorporated bacterial cellulose [124] and N-doped grapheme [125] were also prepared. These Ag catalysts all showed improved ORR activity and stability in the alkaline electrolyte. Inspired from Pt and Pd-based multimetallic electrocatalysts, incorporating other metals into Ag was also studied to improve catalytic performance. Novel octopus-tentacle-like Cu nanowire-Ag nanocrystals were synthesized by growing Ag on Cu NWs in solution phase [126]. The electrocatalytic measurement results demonstrated that the obtained 1D

heterostructures exhibited enhanced ORR performance, which can be ascribed to the presence of multiple junctions and strong synergistic effect of their constituents. 1D Ag/Au/AgCl nanocomposites were prepared by the galvanic replacement between Ag nanowire template and Au precursor [127]. Increasing the concentration of Au precursor induced the structure of the catalysts changes from a core-shell solid wire to a porous hollow wire. The as-prepared catalysts with optimal composition showed comparable ORR activity to commercial Pt/C in alkaline solution.

4.2.2 1D non-precious metal catalysts (NPMCs)

Since cobalt phthalocyanine was initially reported to show catalytic activity for ORR, many attempts have been carried out to explore a variety of non-precious 1D materials for further cost-cutting [128]. However, due to the large difficulties facing the preparation, the research for 1D NPMCs has only been focused on a few special materials.

Transition metal chalcogenide Cu_2Se nanowires [129] with an average diameter of 70 nm have been prepared for ORR applications based on a solid-liquid phase chemical transformation method. The phase structure-property relationship toward ORR was investigated, and it was found that the tetragonal phase Cu_2Se nanowires showed a better ORR performance than that of cubic phase ones. The different phases contribute to the different spatial arrangement ways of Cu and Se atoms, leading to different adsorption and activation of oxygen avenues and resulting in different catalytic performance, which are similar to that for precious metal catalysts.

Besides the transition metal chalcogenides, manganese oxide (MnO_x) has also been considered to be a good non-precious ORR catalyst due to its low cost, environmental friendliness and high activity. MnO_x doped carbon nanotubes (CNTs) [130] were fabricated via a simple electrochemical deposition method and demonstrated an excellent catalytic

behaviour for ORR, resulting from the highly positive charged CNT surface generated by the electron transfer from CNTs to Mn ions (Fig. 6). Ni-α-MnO_2 and Cu-α-MnO_2 nanowires were prepared through the hydrothermal reaction and blended with graphene-like carbon (GLC) to serve as effective catalysts for ORR [131]. The results indicated that the ORR activity of 20% ceramic/80% GLC blends outperformed that of 20% Pt/C. Spinel phase 1D nanostructures, like marokite $CaMn_2O_4$ nanorods [132] and $NiCo_2O_4$ nanowires [133] were also prepared for ORR applications and a comparable mass and specific activity with Pt/C catalyst has been reported in alkaline electrolytes.

(Fig. 6 here)

Recently, N-containing carbon materials such as CNTs have also been intensively studied [134-136] as electrocatalysts for the ORR in acid or alkaline medium. The formed pyridine units embed in a conjugated sp^2 carbon network dramatically improve the catalyst performance [136].

Although all of the above-mentioned 1D non-Pt based catalysts demonstrated acceptable ORR activity or durability, the mass and specific activities were rarely provided, the performance was general evaluated in alkaline environment and still far from the state-of-the-art Pt/C catalysts. Further investigations should be continued to improve the catalytic performance towards ORR, in particular in acid environment for potential PEMFC applications.

5. 1D nanostructured catalysts for hydrocarbon oxidation reaction

Similar to the ORR at the cathode, the oxidation reaction of fuels at the anode also plays a key role on the performance of hydrocarbon fed PEMFCs. Hydrocarbon species such as methanol, ethanol and formic acid are considered to be promising fuels as they can be handled, stored and transported much easier than hydrogen. These hydrocarbons possess

identical advantages such as abundant, inexpensive and high volumetric energy density, at the same time, having their individual characteristics. Among these three fuels, ethanol has the highest energy density and more easily available from fermentation of biomass. However, the oxidation of ethanol is associated with the breaking of C-C bond, which requires a higher activation energy than C-H bond cleavage. Though a bit toxic, methanol is usually used as fuel cell fuel because it has appropriate energy density and doesn't suffer from the problem as its counterpart ethanol. Recently, formic acid also draws a lot of attention due to the reasons that it is a non-toxic and non-flammable liquid fuel and has a smaller crossover flux than methanol through polymer electrolyte membrane. In order to efficiently employ these liquid fuels in PEMFCs, catalysts with excellent catalytic activity and stability for hydrocarbons oxidation are highly desired.

In hydrocarbon fed PEMFCs, the anode reaction suffers from slow kinetics, and requires a high loading of catalysts to achieve acceptable current density, thus a very thick catalyst layer is always expected. 1D nanostructures, due to their anisotropic feature, can interconnect each other to form a network in the electrode thus improving electron transport and catalyst utilization as well as facilitating mass exchange and fuel diffusion during the electrochemical process. As a consequence, 1D nanostructures have attracted huge amount of efforts for hydrocarbon oxidation research in recent years.

5.1 1D Pt-based catalysts for hydrocarbon oxidation reaction

Up to now, Pt-based catalysts are still the most practical catalysts for hydrocarbon oxidation reaction. However, the process of hydrocarbon oxidation usually undergoes formation of carbonaceous molecules such as CO and CHO, which poison the platinum surface and cause irreversible inactivation of the catalysts. Compared with the much rough surface of nanoparticles, 1D Pt-based nanostructures usually possess a much smooth catalyst surface

with less defect, which has a weak adsorption with those carbonaceous molecules [137, 138] thus providing an enhanced poisoning resistance.

5.1.1 1D Pt catalysts for hydrocarbon oxidation reaction

Polycrystaline and single-crystal Pt nanowires [56, 139, 140], nanotubes [13, 58, 141], nanofibers [142] and nanorods [143, 144] have all been tested for hydrocarbon oxidation with a main focus on methanol oxidation reaction (MOR). For example, ultrathin and ultralong single-crystal Pt NWs with a diameter of 3 nm and length of 10 μm were synthesized by using solvothermal method and catalysed for MOR and formic acid oxidation reaction (FAOR) [140]. The mass activities for MOR and FAOR reached ca. 500 and 700 mA mg^{-1} and the specific activities were about 1.15 and 1.5 mA cm^{-2}, respectively. In addition, after 3000 potential cycles, there are only about 31% and 37% activity loss for MOR and FAOR, which is much lower than the degradation rate of Pt/C. Using sacrificial Ag templates via a galvanic replacement process PtAu alloy NTs were also prepared and applied for FAOR [141]. The SEM and HRTEM images in Fig. 7 show the homogeneous dissolution of Pt and Au across the bimetallic alloy and the nanotube morphology with a porous wall. The mass activity of bimetallic PtAu NT series enhanced by 4, 10 and 22 times relative to Pt NT, Pt/C and Pt black, respectively. Through electrochemical deposition route, mesoporous Pt nanorods were also produced with the assistance of surfactant micelles [144]. The 1D motifs demonstrated 209 mA mg^{-1} mass-normalized current density and high CO tolerance in MOR.

(Fig. 7 here)

The synergistic effect between catalyst and support for an improved catalytic performance was also further confirmed towards hydrocarbon oxidation reaction. Many conductive materials including carbon sphere [138, 145, 146], carbon nanotube [147], graphene [68, 147-150] and metal oxide [67] are employed to support 1D catalysts for MOR.

Graphene-branched-Pt hybrid nanostructures (BPtNs) were synthesized by in-situ reduction of graphene oxide and Pt precursor solution using $NaBH_4$ [68], showing a peak current density of ca. 49 and 14 times higher than that of BPtNs without graphene and Pt/C for MOR, respectively. To take a further advantage of this synergistic combination from a hybrid support for an enhanced catalytic performance, Pt NFs decorated graphene-carbon nanotube hybrids (Pt/G-MWNT) were also prepared through electrodeposition method [147]. The obtained catalysts exhibited a high mass activity of 127.43 mA mg^{-1}.

5.1.2 1D Pt-based alloy catalysts for hydrocarbon oxidation reaction

Compared with monometal systems, the unique alloyed catalysts with controlled architectures and compositions also exhibit a superior activity in hydrocarbon oxidation reaction due to the synergistic effect, electronic effect and/or bifunctional mechanism, as those in ORR. Based on these understandings, numerous 1D Pt-based alloy nanostructures have been successfully synthesized and investigated for hydrocarbon oxidation reaction. Prominent examples include 1D PtPd [108, 151-155] and PtAu [105, 141, 156, 157] bimetallic nanocrystals and multimetallic nanoalloys based on them. In recent literatures, Rh [158] and Ru [159] are also employed to construct promising 1D Pt-based alloy catalysts. Besides, non-precious metals such as Fe, Co, Ni, Cu and Bi also have been explored as substitutes for precious metals in 1D Pt-based electrocatalysts [31, 160-167]. Aside from chemical composition, the shape and morphology of alloyed nanostructures were also controlled to further improve the catalytic function and application performance.

It has been recently reported [153] that the incorporation of Pd with Pt can change the MOR process, leading to a non-CO pathway, which is different from the supposed bifunctional effect (e.g. for PtRu alloy) to improve CO tolerance. The modification of the traditionally expected methanol oxidation pathway is ascribed to the decrease of Pt-Pt pair

sites at the catalytic interface. Porous PtPd NDs with an average branch diameter of 19.5 nm demonstrated 3 and 16 times higher enhanced activity than that of Pt black and Pd black towards methanol and ethylene glycol electrooxidation in alkaline solution, and the I_f/I_b (I_f the forward peak current density; I_b the backward peak current density) reached as high as 3.5 [151]. PdPt alloy NWs have also been demonstrated a 1.2 and 1.8 times higher mass activity for ethanol oxidation reaction (EOR) than that of Pd NWs and Pt NTs, respectively [152]. Wong's group [153] demonstrated that a nearly 3-fold improvement of alloyed $Pt_{50}Pd_{50}$ NWs over commercial Pt/C for MOR in acid electrolyte. Recently, bimetallic PtPd porous hollow nanorod arrays (PHNRAs) was reported showing 2.5 times higher current density towards MOR than Pt/C, as well as an outstanding stability confirmed by an almost constant peak current density after 500 potential cycles [154]. The performance improvement is due to the alternative arrangement of Pt and Pd nanocrystals as well as the porous, hollow nanorod structure, which respectively benefits for the modification of electronic structure and facilitates the mass transfer through the catalyst, leading to an efficient catalytic reaction. The images, performance and advantages of PHNRAs are illustrated in Fig. 8.

(Fig. 8 here)

Not like PtPd nanostructures, the combination of Au to Pt nanostructures mainly show enhancement in the FAOR activity [105]. The alloyed PtAu changed the reaction pathway, enhancing the catalytic activity and the tolerance to CO poisoning through ensemble effects and modified electronics induced by compositional variation. The activity of the Pt_1Au_3 NTs for FAOR could be 26, 82, and 149 times higher than that of Pt NTs, Pt black and Pt/C, respectively [141], possessing a peak current density of 1.45 A mg^{-1} and an I_f/I_b ratio of 5.0. Besides, Au-Pt double-walled NTs consist of an Au inner wall and a Pt outer wall have also been reported for MOR application [157].

In addition to Pd and Au, the alloying of other precious metals with Pt has also been reported. Pt/Ru alloy NWs were prepared as high performance catalyst for MOR [159], attributing to the lattice contraction, the enhanced electronic property, along with the facilitated oxidation of adsorbed CO species. With the assist of Rh nanocubes as seeds, ultrathin Rh/Pt NWs were synthesized and employed for EOR [158]. The Fourier transform infrared spectroscopy (FTIR) investigation for the reaction intermediates of EOR showed that Rh had a special effect on cleavage of C-C bond in ethanol and the alloyed catalyst possessed a high selectivity to the complete oxidation of ethanol to CO_2.

Bring a step forward from the precious metals, alloying Pt with less expensive transition metals can not only promote the formation of 1D morphology, but also increase the oxidation of intermediate species, thus changing Pt d-band centre, promoting C-H cleavage and the mitigation of CO oxidation at lower potential for an improved hydrocarbon oxidation. The excellent activity of 1D PtNi alloy nanostructure towards ORR also makes it a promising candidate for hydrocarbon oxidation. PtNi NDs [160], NWs [162], NRs [163], NTs [166] have been investigated for FAOR, MOR and EOR, respectively. It was also found that the addition of phosphorus (P) to PtNi can significantly improve the relative content of Pt(0) and the 5d electron density of Pt for an enhanced catalytic activity. The specific current density of Pt-Ni-P nanotube arrays (NTAs) for MOR reaches 3.85 mA cm^{-2}. The SEM image, scheme of MOR process in Pt-Ni-P NTAs and corresponding electrochemical activity and durability are shown in Fig. 9 [166]. Other transition metal alloyed 1D Pt nanostructures recently studied include PtBi [31] and wormlike Pt-M (M=Cu, Co, Fe) NWs [162] from wet chemical approaches, as well as PtCo NWs [161], PtCu [164] and PtCo [165] NTs synthesized with the aid of templates. All of them demonstrated an increased catalytic activity and a high CO poisoning resistance towards EOR or MOR.

(Fig. 9 here)

The outstanding catalytic performance of PtPd for MOR also makes it a potential base to develop multimetallic alloy nanostructures to further improve its catalytic activity. Fe, Te and Au alloyed PtPd NWs showed a significant increase in peak current density, a negative potential shift in methanol oxidation and a slow decay rate in durability test [168-170]. PtPdTe NWs with a diameter of 5–7 nm exhibited a high electrocatalytic activity of 595 mA cm^{-2} mg^{-1} towards MOR, which is 2.4- and 2.6- fold higher than that of PtTe NWs and Pt/C, respectively [169].

5.1.3 1D Pt-based hybrid catalysts for hydrocarbon oxidation reaction

Due to the slow kinetic activities facing by hydrocarbon oxidation, the current efforts are mainly carried out on the improvement of catalytic activities, e.g. through alloy nanostructures as mentioned above. As the same, the work conducted here via using hybrid catalysts still focuses on enhancing catalytic activities rather than simply reducing the cost as that for ORR.

Pt/PtCu core-shell NTs with a wall thickness of 20 nm were prepared through a galvanic replacement approach for FAOR application [171]. The merits of tailorable electronic structure of core-shell nanostructure contributed to 4 and 10 times higher catalytic activity and durability than that of Pt/C, respectively. By UPD replacement method, Pt on Pd NWs [172] and Pt decorated Ru NWs [173] with a respective diameter of 10–20 nm and 40–280 nm were obtained and applied to hydrocarbon oxidation. The peak current density of Pt on Pd NWs for EOR was 858.6 mA cm^{-2} in alkaline medium. Pt decorated Ru NWs maintained a high degree of performance for MOR compared with traditional 0D PtRu NP/C and Pt/C catalysts, exhibiting a mass activity of 360 mA mg^{-1} and a specific activity of 0.36 mA cm^{-2} in $HClO_4$ electrolyte. The functionality of Au for anti-poisoning component of Pt also enables 1D Au/PtM core-shell nanostructures a possible electrocatalyst for hydrocarbon

oxidation. Core-shell Au-Pt NWs [25] were generated by controlled coverage of Pt shell layers on the surface of Au nanowire cores which were obtained through surfactant-mediated M13 bacteriophage template. The corresponding TEM and STEM images are shown in Fig. 10. The enhanced intrinsic activity for EOR and the chronoamperometry measurement results indicated the advantage of core-shell nanowire catalysts over the commercial Pt/C catalysts. Going one step further, alloying the surface Pt with Au to prepare core-shell Au/PtAu NRs [105] has been explored for FAOR, and the results demonstrated that the enrichment of Au on the surface also showed a positive effect. Porous Ni@Pt core-shell NTs with a wall thickness of 105 nm were also synthesized by ZnO nanorod template assisted electrodeposition method for MOR and a 3.7 folds higher steady-state current density than that of Pt/C catalyst was achieved [174].

(Fig. 10 here)

Apart from core-shell structure, Pt-Pd heteronanostructures have also been studied. Wang et al. [175] prepared Pt-on-Pd bimetallic NDs with an average diameter of 10 nm and demonstrated a better catalytic performance for MOR than either the Pt NDs or Pt black, showing a mass activity of 490 mA mg^{-1}. Pt decorated coral-like Pd nanochains [176] with a diameter of 5.2 nm were successfully synthesized through a facile wet-chemical method and applied for FAOR, showing a peak current density 4.4 times higher than that of Pt/C and an improved durability as well.

5.2 1D non-Pt based catalysts for hydrocarbon oxidation reaction

Besides the high cost, the surface of Pt is usually heavily poisoned by the strong adsorption of CO intermediates in hydrocarbon oxidation, resulting in the deterioration of catalytic performance. This challenge forces both academic and industrial communities to find Pt substitutes and numerous investigations have been conducted to explore alternative high

performance electrocatalysts. In recent years, this topic focused on Pd [177-183] and Pd-based catalysts [184-192] due to the great abundance of Pd in nature and its lower cost than Pt. Particularly, unlike its counterpart Pt, Pd-based catalysts are less suffered from poisonous CO intermediate species and have a lower oxidation overpotential towards hydrocarbon electrooxidation, thus regarding as one of the most promising Pt-free catalysts for the electrooxidation of hydrocarbon molecules. The only Pd free catalysts reported are Ni-Cu alloy porous NWs prepared for MOR in alkaline solution [193].

Pd NWs [178-180], nanochains [181], nanothorns [182] and more complex flower-like nanostructured networks [177], as well as Pd/polyaniline/Pd sandwich structured nanotube arrays (SNTAs) [183] have been studied. Xia's group [180] synthesized 2 nm ultrathin Pd NWs via a polyol method and the electrochemical measurement showed a catalytic current density of 2.5 folds higher than that of Pd/C catalysts towards FAOR. Hong et al. [178] and Wang et al. [179] reported that the mass activity of Pd NWs with a diameter of 4–5 nm reached 1.45 and 1.1 A mg^{-1} for EOR and FAOR, respectively.

The main efforts for 1D Pd-based alloy catalysts towards hydrocarbon oxidation were on precious alloyed catalyst, especially 1D Pd-Au bimetallic nanocrystals. Pd-Au alloy NDs [184, 185], Au@Pd core-shell NDs [186] and PdAu nanowire networks [187] were all synthesized through the wet-chemical reduction method by using different reductants and stabilizing agents. By controlling the nucleation and growth rate, the produced catalysts with the diameter ranges between 3 and 26 nm demonstrated good catalytic performance for MOR or EOR in alkaline media. The excellent performance can be ascribed to the improved electron transport characteristics, the increased active sites as well as the favoured adsorption of OH_{ads} onto the catalyst surface, which collectively improve the catalytic process. Besides, PdAg alloy NWs with an average diameter of 5–8 nm were obtained by coreduction method [188] and nanoneedle-covered PdAg NTs [189] were synthesized via a galvanic displacement

of Ag nanorods for FAOR,. Rh-on-Pd bimetallic NDs composed of Pd cores and 15–30 nm Rh branches were also synthesized with ethylene glycol and CTAB for EOR application [190]. Apart from combining with precious metals, some works were also reported for 1D Pd alloyed with non-precious metals. Nanoporous PdNi [191] and PdBi [192] alloy NWs were synthesized for FAOR application. Quinary PdNiCoCuFe alloy nanotube arrays have also been prepared by template-assisted electrodeposition method for MOR and EOR in alkaline solution [194].

6. PEMFC electrodes from 1D Pt nanostructures

Owing to the large aspect ratio, Pt NWs can form into free-standing membrane by interconnected network, which possesses characteristics of high porosity, good flexibility and large area per unit volume compared with the conventional catalyst membrane. Yu and co-workers [195] prepared free-standing Pt nanowire membrane by using Te@C nanocables as templates for the formation of Pt@C nanocables via the galvanic replacement reaction between Te and $PtCl_6^{2-}$, followed by a calcination at 400 °C in air. The Pt nanowires produced by this approach had a large size of 12 nm, resulting in only a 50% ECSA of Pt/C catalyst (40 wt% Pt, JM). However, with the unique surface properties of long crystalline Pt NWs, together with the nanowire network structure wh Int. J. Low-Carbon Technol ich facilitated the electron transport and gas diffusion, the free-standing Pt nanowire membrane exhibited a comparable mass activity and a much improved durability for the ORR compared with the Pt/C catalysts.

Although the considerable progress has been achieved for catalysts themselves, especially on novel nanostructured catalysts, an increasing gap exists between the pure material research and practical fuel cell application. Until now, Pt nanowire is still the only 1D nanostructure that has been tested in PEMFCs. Due to the unusual morphology, catalysts

with novel nanostructures are usually very difficult to fabricate into fuel cell electrodes by a conventional process as used for Pt/C electrodes. This challenge also faced by 1D Pt nanostructures. Carbon supported Pt NWs have been fabricated into PEMFC cathodes using the conventional approaches (e.g. painting, printing, screening, etc.) and tested in single cells [196-199]. A test was also conducted within a 1.5 kW PEMFC stack under collaboration between Tongji University, University of Waterloo and General Motors [198]. Both power performance and durability were evaluated. Although Pt NWs showed a larger diameter (ca. 4 nm) compared with the conventional Pt nanoparticles, a similar power performance was still achieved benefiting from the unique catalytic activity of Pt NWs and the reduced mass transfer losses in electrodes with enhanced porosity. The characterisation for the catalysts before and after the durability test further indicated the enhanced stability of Pt NWs over Pt/C. However, the large porosity also resulted in a thicker catalyst layer and a loose electrode structure in PEMFCs. Although an excellent stability was observed for Pt nanowire catalysts themselves, the poor electrode structure could still not bring a significant improvement to the electrode durability, and finally only a slight improvement was obtained. After a 420 h dynamic drive cycle durability testing, PEMFC stacks exhibited a performance degradation rate of 14.4% and 17.9% for PtNW/C and commercial PtNP/C based cathodes, respectively, which is shown in Fig. 11 [198]. The authors ascribed the majority of performance loss to the degradation of the commercial Pt/C anode materials. However, considering the much easier hydrogen oxidation reaction and the high catalyst loading of 0.2 mg_{Pt} cm^{-2} used in the anode, this performance loss should be mainly ascribed to the degradation of the cathode structure, as pointed out by Holdcroft in his review on fuel cell catalyst layers [200].

(Fig. 11 here)

One important progress in PEMFC electrodes in recent decades is the concept of the thin film catalyst layer, which was introduced by the 3M Group in its nanostructured thin film (NSTF) catalyst electrode. The catalyst layer consists of a monolayer array of perylene whiskers (1 μm tall, 30 nm×55 nm in cross-section) with a surface coated 20 nm polycrystalline PtCoMn film, which was achieved by a decal substrate transfer approach [201, 202]. SEM images of the PtCoMn alloy catalyst sputter coating on the microstructured substrate supported whiskers before transferring are shown in Fig. 12. This thin film catalyst layer with a regular structure enabled a much higher catalyst utilization ratio in the electrode to meet the U.S. DOE targets of mass activities. However, the approach is intrinsically limited by challenges facing water management issues in practical operation and the very low ECSA (only 10–15 m^2 g_{Pt}^{-1}), as well as the catalyst materials and structures used. Recently, Cullen et al. [203] investigated the structure-property relationship of PtNi NSTF catalysts under fuel cell testing conditions. They demonstrated that catalyst pre-treatments, conditioning and potential cycling could influence the structure and composition of the extended surface catalysts, which could further affect their surface area, activity and durability.

(Fig. 12 here)

Another advance on thin film electrodes was achieved by Du and his colleagues [204-207]. Integrated gas diffusion electrodes (GDEs) were prepared by in-situ growing single crystal Pt nanowires on gas diffusion layer (GDL) surfaces, taking the advantages of the unique simplicity of the formic acid reduction approach at room temperature [35]. The GDL was directly used as support substrate. The whole catalyst layer contains only a monolayer array of single-crystal Pt nanowires with a diameter of ca. 4 nm and a length of 20–200 nm. The obtained structure could be directly used as fuel cell electrodes. The extremely thin catalyst layer with a regular structure further reduced the mass transfer losses and improved the catalyst utilization; and the removal of the carbon support in Pt/C potentially contributed

to the improvement of the electrode durability, both of which have been considered as the challenges faced by PEMFCs in automotive applications [201]. However, due to the hydrophobic surface of Pt nanowires, Nafion ionomer was still required for the catalyst layer to conduct protons within the PtNW electrodes, which has been successfully removed from the NSTF catalyst electrodes due to the hydrophilic pores which led to water flooding thus facilitating proton transfers [206]. Furthermore, a well-controlled structure of the catalyst layer is also of great importance to control triple phase boundary (TPB) for a higher catalyst utilization ratio. The results demonstrated that an optimal Pt loading was necessary to achieve a better performance as a low Pt loading could not cover the entire GDL surface while a high loading resulted in little void volume for gas diffusion [205].

It was also found that even with the same Pt nanowires, their distribution on the GDL also has a large impact on the final electrode performance. An optimal in-situ growing temperature can partially balance the contact between the aqueous reaction solution with the superhydrophobic GDL surface, improving the distribution of Pt nanowires on GDL surface and enabling a better electrode structure [208]. A nearly double mass activity and three times higher specific activity were achieved over the TKK Pt/C catalyst (45.9 wt% Pt/C, TEC10E50E) by testing using a standard protocols in hydrogen-oxygen fed PEMFCs as defined by Gasteiger et al. [209]. The ADT of cathode also confirmed a better durability of Pt nanowire electrodes with 48% loss in the ECSA compared with 67% loss of Pt/C nanoparticle electrode. In order to reduce the diameter of Pt NWs in GDEs to increase the ECSA and thus further enhance the electrode performance, active screen plasma nitriding (ASPN) was introduced to treat the GDL surface before Pt NW growth [210]. The nitrogen doping on GDL surfaces introduced in ASPN confined the Pt atoms in reaction to form tiny nuclei and finally produced ultrathin Pt nanowires with a diameter of only 3 nm, offering a larger ECSA for a better catalytic activity. Furthermore, the functional groups introduced by

ASPN on the GDL surface facilitated the contact between the substrate surface and the reaction solution to form a much uniform distribution of nanowires, further improving the catalyst utilisation ratio. Images of Pt nanowires grown on the ASPN-treated GDLs are shown in Fig. 13. The cathode cyclic voltammogram (CV) showed a larger Pt oxide reduction potential, further confirming the weakening of the bond between oxygen containing species and the surface of Pt nanowires which also contributed to a better ORR performance. The testing of a PtNW cathode with only half catalyst loading showed an even better power performance than the electrode with Pt/C nanoparticles. Inspired by the work from Xia's group [211], we introduced Pd nanoseeds on GDL surface to direct the growth of Pt nanowires [212]. This successfully improved the distribution of catalyst nanostructures on GDL surface, reducing the mass transfer losses in catalyst layer and the electrode achieved a higher power performance at 0.6 V. However, the introduced nanoseeds also led to the formation of dendrite-like Pt nanostructures, resulting in a less catalyst mass activity and poorer durability compared with pure Pt nanowire electrodes.

Collaborated with Sui's group, this PtNW catalyst electrode was also fabricated by in-situ growing Pt NWs on the carbon coated Nafion membrane or PTFE surface followed by a transfer step to Nafion membrane surface, which are similar to the catalyst coated membrane (CCM) and decal methods used in the fabrication of conventional Pt/C electrodes, respectively [213-215]. In this case, a better contact between the catalyst and the polymer electrolyte membrane (PEM) can be realized to achieve a better power performance. The preliminary tests confirmed a better performance compared with Pt/C electrodes and also the importance of Pt NW distribution in controlling the electrode structure.

However, although an excellent power performance with a high catalyst utilisation ratio has been demonstrated with these electrodes with PtNW arrays, a water flooding may happened in operation due to the extremely thin catalyst layer, as that has been reported with

NSTF catalyst electrodes [201]. The unique hierarchically micro/nano-structured interface within this PtNW catalyst layer can provide a superhydrophobic feature [216] that can potentially address the water management challenges. A long-term stability testing, in particular within PEMFC stacks, is urgently required to confirm the real potential of this advanced approach.

(Fig. 13 here)

7. Summary and Perspective

An impressive progress has been achieved in recent years in the design and synthesis of 1D nanostructured materials as active and durable electrocatalysts for potential applications in low temperature fuel cells. Owing to the inherent properties, 1D nanostructured electrocatalysts have the potential to resolve many issues associated with their 0D counterparts and are regarded as the promising candidates for the replacement of contemporary 0D catalysts. A summary of these 1D nanostructures is listed in Table 1 by a comparison between their structure, preparation approach, performance measurement method and activities.

Among all the 1D catalysts, Pt-based nanocomposites are still the most practical catalysts due to their good electrocatalytic activity and durability. However, the rational design of self-supported, highly active and long-time lasting catalysts is still a challenge, especially when taking into account the complex reaction mechanism and harsh fuel cell operational conditions. Although great efforts have been devoted to fabricate non-Pt or even non-precious metal based catalysts to reduce the production cost, they usually suffer from dissolution in acidic electrolyte and most of them can only performed in alkaline medium. At present, numerous work are focusing on fabricating advanced catalysts possessing combined merits of 1D morphology, multi-composition as well as novel structures like core-shell,

porous, hollow and ultrathin shape. Nonetheless, it seems there is no in-depth understanding about the function of these factors at molecule reaction level. We also need to pay attention to that the majority of the evaluation processes for 1D nanostructures is only based on ex-situ electrochemical measurement in liquid electrolyte, and only Pt nanowires have been really tested in fuel cells, which is crucial for practical applications.

In light of these shortfalls, future work should focus on the following aspects: (i) an emphasis must be placed on the validation of catalyst performance in real fuel cell operating conditions as catalyst will experience a much different and crucial environment in real fuel cell conditions. A gap between pure material research and practical fuel cells resulted in that many new nanostructure approaches developed only stayed at the "test tube" level and did not work in fuel cells. If the 1D catalysts with excellent catalytic activities can be fully approved with fuel cells, the targets for commercialisation can be easily met; (ii) more in-depth theoretical and experimental studies are demanded to understand the structure-property correlations in electrocatalysis, in particular in fuel cell electrodes. The unusual shape of 1D nanostructures requires new understanding to develop innovation approach to fabricate them into fuel cell electrodes, rather than using conventional processes for Pt/C nanoparticles; (iii) the approach for electrodes with in-situ grown monolayer array of Pt nanowires could be a promising technology. However, this can only happen after the long-term stability and water management issues have been confirmed. Based on the much enhanced mass transfer performance and catalyst utilization ratio, if the synergistic effects of the alloy and hybrid nanostructures can be brought into the structure, it could offer a new path for the design and development of PEMFC electrodes; (iv) an ongoing pursuit should be performed to develop facile, green and scale-up catalyst synthesis processes to realize high-yield catalyst production, in particular for the approaches leading to a reduced precious metal loading, i.e. 1D non-precious group metal catalysts which could play a special role in meeting the

requirement for fuel cell commercialisation; (v) continuous efforts should be made to understand the fundamental catalytic mechanisms of 1D nanostructures, including the appropriate adsorption for reactant species and favourable electron transfer pathway to optimize the geometry, composition and structure for a further improvement of the catalytic activity and durability. It is believed that with the resolving of these challenges, 1D nanomaterials with novel structural motifs, diverse advantages, multifunctional performance and effective cost will show a high potential for low temperature fuel cell applications.

Table 1. Summary of one-dimensional (1D) nanostructured catalysts for PEMFCs

Catalyst	Preparation	Morphology	Measurement	Activities	References
Oxygen Reduction Reaction					
Pt NWs	Wet chemical synthesis	Diameter: 1.3–3 nm; length up to several micrometers	ORR	88 mA mg^{-1} 0.368–1.45 mA cm^{-2}	[17, 55, 56]
Pt nanowire membrane	Te nanowire template	Diameter: 12 nm; length: hundreds of nanometers	ORR	Comparable with JM Pt/C	[195]
Pt NTs	AAO, Ag or Cu nanowires templates	Wall thickness: 2.5–11 nm	ORR	84.5–240 mA mg^{-1} 0.369–2.39 mA cm^{-2}	[13, 57-60]
Pt NRs	Glancing angle deposition (GLAD) technique	Diameter: 5 up to 100 nm; length: 50–400 nm	ORR in $HClO_4$	Lower mass but higher specific activity than Pt/C	[61]
Pt nanochain or nanolance	Thermal decomposition or hydrothermal methodology	Diameter: 5–15 nm	ORR	3.24 mA cm^{-2}	[62, 217]
Single Pt NW electrode	UPD or lithography patterning	Radius: 6–130 nm; length: 40 nm.	ORR in KOH and H_2SO_4		[53, 54]
Supported Pt NWs	Spray drying and formic acid reduction	Diameter: 4–13.9 nm	ORR in acid	33–158 mA mg^{-1} 0.415 mA cm^{-2}	[65-67]
Pt NWs/graphene	$NaBH_4$ or formic acid reduction	Diameter: 2–5.8 nm	ORR in acid	1010 mA mg^{-1} 1.5 mA cm^{-2}	[68-70]
Pt NWs/C	Acid reduction or electrospinning	Diameter: 4.0–85 nm	H_2/air PEMFC cathode	Max power density: 748.8 mW cm^{-2}	[196, 197, 199]
Pt NW arrays	Formic acid reduction	Diameter 4 nm	DMFC cathode	64 mW cm^{-2} at 2 mg cm^{-2} Pt loading	[210]
Pt NW arrays	Formic acid reduction	Diameter: 4 nm	Integrated PEMFC cathode	max power density: 340–390 mW cm^{-2}	[204, 213]
Pd-Pt ND, NW and NR	Chemical and template approach	Diameter: 10–35 nm	ORR in $HClO_4$ and KOH	up to 3810 mA cm^{-2}	[75-77, 79, 108, 218]
Pt-Au NRs	Formic acid reduction	Diameter:10–20 nm	ORR in $HClO_4$	48 mA mg^{-1}	[77, 79]
Pt-Fe NWs	Electrospinning / organic phase reduction	Diameter: 2.5–10nm	ORR in acid	77.1–844 mA mg^{-1} 0.3831.53 mA cm^{-2}	[82-84]
CoPt NWs	Organic phase reduction	Diameter: 2.5 nm;	ORR in $HClO_4$	0.64 mA cm^{-2}	[84]
PtNi NR or NF	Sputtering/template	Diameter: 25–100 nm	ORR in $HClO_4$	440 mA mg^{-1} 1–4.41 mA cm^{-2}	[86, 219]

Pt-Cu NTs	AAO template/ galvanic replacement	Wall thickness: 30.3 nm	ORR in $HClO_4$	190–232 mA mg^{-1} 0.8–2.57 mA cm^{-2}	[88, 90]
Pt-Cu NRs	Polyol or formic acid reduction	Diameter: 5 nm; length: 6–20 nm	ORR in $HClO_4$	44–48 mA mg^{-1} 0.215 mA cm^{-2}	[77, 93]
PtNiFe NWs or NRs	Organic phase	Diameter: 2 nm; length: 20 nm	ORR in acid	5.32 mA mg^{-1} 0.0077 mA cm^{-2}	[91, 92]
PtCuM NRs and NTs (M=Ni, Fe, Pd)	Wet chemical /template	Diameter: 2–30 nm; length: 20 nm	ORR in $HClO_4$	64–103.4 mA mg^{-1} 0.25–1.37 mA cm^{-2}	[92-94]
PtCuCoNi NTs	AAO templates	Wall thickness: 30–10 nm	ORR in $HClO_4$	190 mA mg^{-1} 0.18 mA cm^{-2}	[95]
Pt coated Cu NWs PtCu/Cu NWs	Galvanic displacement	Outer diameter: 100 nm; Pt layer: 2 nm	ORR in $HClO_4$	82 mA mg^{-1} 1.50 mA cm^{-2} 1240 mA mg^{-1}, 2.65 mA cm^{-2}	[60, 85]
Pd-Pt core-shell NWs, NTs	UPD or galvanic displacement	Core diameter: 2.0 nm; wall thickness: 6 nm	ORR in $HClO_4$	340–1830 mA mg^{-1} 0.58–0.77 mA cm^{-2}	[99, 101-103]
Au/Pt or PtM (M=Au, Ni) NWs and NRs	Chemical reduction		ORR in acid	41.3–479 mA mg^{-1} 0.308 mA cm^{-2}	[80, 105, 107]
Pt-PdAu core-shell NW	UPD and galvanic replacement	Diameter: 2.5±0.3 nm; length: several tens of nanometers	ORR in $HClO_4$	2600 mA mg^{-1} 1.0 mA cm^{-2}	[104]
FePtM/Pt or FePt (M=Pd, Au) NWs or NRs	Chemical reduction	Shell thickness: 0.3–1.3 nm	ORR in $HClO_4$	103.4–1680 mA mg^{-1} 1.369–3.47 mA cm^{-2}	[92, 106]
Pt-on-Pd NDs	Ascorbic acid reduction	Branch width: 2–3 nm	ORR in H_2SO_4	36.5 mA mg^{-1} 0.342 mA cm^{-2}	[109]
Pt-on PdBi NW	Oil phase synthesis	Diameter: 8.3 nm;	ORR in $HClO_4$	1160 mA mg^{-1} 1.48 mA cm^{-2}	[110]
Pd NWs	Template method	Diameter: 45 nm,	ORR in $HClO_4$	1.84 mA cm^{-2}	[111]
PdCu NWs	Colloidal method	Width: 18.2 nm	ORR in $HClO_4$		[114]
PdFe nanoleaves	Wet chemical method	Diameter: 2.3 nm	ORR in NaOH	159 mA mg^{-1} 0.305 mA cm^{-2}	[115]
Core-shell MnO_2@Pd-NRs	Electroless deposition	Diameter: 40–50 nm	ORR in KOH	500 mA mg^{-1}	[116]
Au NDs/Graphene	Wet-chemical	Diameter: 35 nm	ORR in KOH		[117]
Pd-Au NTs	Galvanic displacement	Wall thicknesses: 6 nm	ORR in KOH	240 mA mg^{-1} 1.98 mA cm^{-2}	[113]
PdAu NWs	Template or wet-chemical	Diameter: 2–50 nm;	ORR in $HClO_4$	0.4–0.49 mA cm^{-2}	[118, 119]
PdAu nanochain	Template	Diameter: 5.6 nm;	ORR in NaOH		[120]
Au@Pd core-shell nanothorns	Co-chemical reduction	Diameter: 30–50 nm	ORR in KOH		[121]
Ag nanobelt	Hydrothermal method	Thickness: 40–60 nm;	ORR in NaOH		[122]

Ag NRs	Polyol process	Diameter: 83 nm	ORR in KOH		[123]
Ag NWs/MWCNTs	Polyol process				[124]
Ag NWs/ N-graphene	Hydrothermal method		ORR in KOH		[125]
Ag/Au/AgCl nanocomposites	Galvanic replacement	Ag NW diameter: 500–550 nm	ORR in NaOH		[127]
Cu-Ag NWs	Seed-mediate	Diameter: 16 nm;	ORR in KOH		[126]
Cu_2Se nanowires	Solid-liquid phase chemical transformation	Diameter:50–70 nm	ORR in KOH	3.5–12 mA mg^{-1}	[129]
N-CNTs	Wet chemical and annealing		ORR in H_2SO_4 and KOH		[135, 220]
N-Fe/Fe_3C@C	Wet chemical and annealing	Diameter: 20–30 nm;	ORR in PBS		[128]
MnO_x-CNTs	Electrochemical deposition		ORR in KOH		[130]
MnO_x NWs	Polyol method	Diameter: 10 nm	ORR in KOH		[221]
Graphene-Ni-MnO_2 and Cu-MnO_2 NWs	Hydrothermal method		ORR in alkaline		[131]
$CaMn_2O_4$ NRs	Solvothermal method	Diameter: 150–300 nm;	ORR in KOH	70 mA mg^{-1} 0.0148 mA cm^{-2}	[132]
$NiCo_2O_4$ NWs	Coprecipitation	Diameter: 50 nm	ORR in KOH		[133]
$RuVO_x$ NWs	Vapor–phase transport	Dimension: 182	ORR in PBS		[222]
Hydrocarbons Oxidation Reaction					
Pt NDs	Formic acid reduction	Width: 2.5 nm	FAOR in H_2SO_4	66.3 mA mg^{-1} 1.2 mA cm^{-2}	[139]
Pt NFs	Electrodeposition	200 nm	EOR in $HClO_4$	1.414 mA cm^{-2}	[142]
Ultrathin Pt NW network	Biomimetic	Diameter: 2 nm	MOR in H_2SO_4	580.97 mA mg^{-1}	[56]
Pt NWs	Solvothermal	Diameter: 3 nm	MOR FAOR in H_2SO_4	MOR: 500 mA mg^{-1} 1.15 mA cm^{-2} FAOR: 700 mA mg^{-1} 1.5 mA cm^{-2}	[140]
Pt NTs	Galvanic displacement with Ag NWs	Wall thickness: 5 nm;	MOR in $HClO_4$ FAOR in H_2SO_4	FAOR: 354 mA mg^{-1}	[13, 58, 141]
Pt NRs	Electrochemical route	Top diameter: 5 nm	MOR in H_2SO_4	47 mA cm^{-2}	[143]
Mesoporous Pt NRs	Electrochemical route	Diameter: 50–120 nm Length: 0.6–3.2 μm	ORR MOR in $HClO_4$	209 mA mg^{-1}	[144]
Branched Pt/graphene	$NaBH_4$ reduction	Average size: 5.8 nm	MOR in H_2SO_4	178.1 mA cm^{-2}	[68]
Pt NFs/graphene - CNTs	Electrodeposition	Size: 60–90 nm	MOR in H_2SO_4	127.43 mA mg^{-1}	[147]

Pt NWs/C	Phase transfer method	Average diameter: 2.5 nm	MOR in H_2SO_4	Peak 0.96 mA cm^{-2}	[138]
Pt NWs/C	Formic acid reduction	Diameter: 4 nm	MOR in H_2SO_4	462.7 mA mg^{-1} 0.8 mA cm^{-2}	[145, 146]
Pt NWs/rGO	Formic acid reduction	Diameter: 4 nm;	MOR in H_2SO_4	1.154 mA cm^{-2}	[149]
Pt NWs/S-Graphene	Formic acid reduction	Diameter: 2–5 nm;	MOR in $HClO_4$	1.6 mA cm^{-2}	[148]
Pt NWs/ $Ti_{0.7}Ru_{0.3}O_2$	Formic acid reduction	Diameter: 4 nm	MOR in H_2SO_4	92.4 mA cm^{-2}	[67]
Pd-Pt NDs	Wet chemical	Average diameter: 19.5 nm	FAOR and MOR in KOH		[108, 151]
PdPt NWs	Template	Diameter: 10.8–50 nm	MOR EOR in NaOH and $HClO_4$	MOR: 1.25 mA cm^{-2}	[152, 153]
PtPd porous hollow nanorod arrays	ZnO template	Wall thickness: around 30 nm	MOR in H_2SO_4	1200 mA mg^{-1}	[154]
PtPd NDs/rGO	Soft template	Diameter: 100.32	MOR EOR in KOH	MOR:333 mA mg^{-1} EOR: 298 mA mg^{-1}	[155]
PtAu NWs	Wet chemical		FAOR	1886.2 mA mg^{-1}	[156]
Pt-Au core/shell NRs	Formic acid reduction	Diameter:4 nm; length: 10–25 nm	FAOR in H_2SO_4	80 mA cm^{-2}	[105]
PtAu alloy NTs	Galvanic replacement	Wall thickness: 5±1 nm	FAOR in H_2SO_4	Peak 1445 mA mg^{-1}	[141]
Au-Pt double-walled NTs	Galvanic replacement		MOR in H_2SO_4	Peak 138.25 mA mg^{-1}	[157]
Rh/Pt NWs	Seed displacement	Diameter: 4.3 nm	EOR in $HClO_4$	Peak 1.2 mA cm^{-2}	[158]
Pt-Ru NWs	Soft template	Average diameter: 3.0 nm	MOR in $HClO_4$	Peak 30.95 mA cm^{-2}	[159]
PtNi/C NDs	Thermal decomposition	Average size: 21.7 nm	FAOR in $HClO_4$	Peak 0.905 mA cm^{-2}	[160]
Pt-Bi NWs	Polyol process	Diameter: 3.6 nm	EOR in $HClO_4$	Peak 0.0138 mA cm^{-2}	[31]
PtCo NWs	AAO template	Diameter: 280 nm	MOR in H_2SO_4		[161]
PtM (M=Cu, Ni, Co, Fe) NWs	Hydrothermal method	Average diameter: 3.1, 2.9, 2.8, and 2.3 nm	MOR in H_2SO_4	1.34 mA cm^{-2}	[162]
PtNi NRs	Dealloying	Diameter: 200 nm;	EOR in H_2SO_4		[163]
Pt-Cu alloy NTs	AAO template	Wall thickness: 45 nm	EOR in H_2SO_4	Peak 32 mA cm^{-2}	[164]
PtCo NTs	Co nanowire template	Wall thickness: 8nm;	MOR in H_2SO_4	Peak 636.4 mA mg^{-1} 2.73 mA cm^{-2}	[165]
Porous PtNiP NTs	ZnO template	Wall thickness: 70 nm	MOR in H_2SO_4	3.85 mA cm^{-2}	[166]
PtPdM NWs (M=Fe, Te or Au)	Thermal decomposition or template	Diameter: 2.5–10 nm	MOR in acid and EOR in NaOH	488.7 mA mg^{-1}	[168-170]
Pt/Pd NWs and NCs	CUPD or Wet chemical	Diameter: 5–20 nm	EOR in KOH MOR and FAOR in acid	EOR: 858.6 mA cm^{-2} MOR: 490 mA mg^{-1} FAOR: 7.62 mA cm^{-2}	[172, 175, 176]
Pt/Ru NWs	CUPD	Diameter: 40–280 nm	MOR in $HClO_4$	360 mA mg^{-1} 0.36 mA cm^{-2}	[173]

Au-Pt core-shell NWs	Virus-template	Diameter: 10–50 nm; length: 5 μm	EOR in KOH	0.72 mA cm^{-2}	[25]
Porous Ni@Pt Core-Shell NTs	ZnO template	Wall thickness: 105 nm	MOR in H_2SO_4		[174]
Pt/PtCu core-shell NTs	Galvanic replacement	Wall thickness: 20 nm	FAOR in H_2SO_4	6.2 mA cm^{-2}	[171]
Pd flower-like networks	CO-assisted reduction	Flower diameter: 96.8 nm	FAOR in $HClO_4$		[177]
Pd NWs	Chemical reduction	Diameter: 2–5 nm	EOR in NaOH FAOR in acid	EOR: 1450 mA mg^{-1} 13.5 mA cm^{-2} FAOR: 1100 mA mg^{-1} 1.38-2.4 mA cm^{-2}	[178-180]
Pd nanochains	KBH_4 reduction		FAOR in H_2SO_4	283.81 mA mg^{-1}	[181]
Pd thorn clusters	Electrodeposition	Diameter: 30–70 nm	FAOR in H_2SO_4		[182]
Pd/PANI/Pd Sandwich-Structured NTs	ZnO template	Wall thickness: 50 nm	EOR in NaOH	Peak 350 mA mg^{-1}	[183]
Au-Pd NDs	Chemical reduction	Diameter: ca. 21 nm	MOR and EOR in KOH	Peak MOR: 27.04 mA cm^{-2} Peak EOR: 4.18 mA cm^{-2}	[184, 185]
Au@Pd core-shell NDs	Ascorbic acid reduction	Arm diameter: 3–7 nm	MOR in KOH	90 mA mg^{-1}	[186]
PdAu and PdAg NWs	Chemical reduction	Diameter: 5 nm;	EOR in KOH and FAOR in $HClO_4$	EOR: 10.8 mA mg^{-1} Peak FAOR: 8.5 mA cm^{-2}	[187, 188]
Pd-Ag NTs	Ag nanorod template	Diameter: 83 nm	FAOR in $HClO_4$		[189]
Rh-on-Pd NDs	Ethylene glycol reduction	Diameter: 15 nm	EOR in KOH	Peak 30–40 mA mg^{-1}	[190]
PdNi NWs	Dealloying	Diameter: 150 nm	FAOR in H_2SO_4		[191]
PdBi NWs	Thermal decomposition	Diameter: 5.7 nm	FAOR in $HClO_4$		[192]
PdNiCoCuFe NTs	Template	Wall thicknesses: 150 nm	MOR in NaOH	100 mA mg^{-1}	[194]
Porous Ni-Cu alloy NWs	Hydrothermal reaction and thermal decomposition	Length: 2 μm	MOR in NaOH		[193]

Acknowledgements

YX Lu was supported by a joint Li Siguang Scholarship from the University of Birmingham (UoB) and the China Scholarship Council (CSC).

References

[1] O.Z. Sharaf, M.F. Orhan, Renew. Sust. Energ. Rev. 32 (2014) 810-853.

[2] Y. Wang, K.S. Chen, J. Mishler, S.C. Cho, X.C. Adroher, Appl. Energ. 88 (2011) 981-1007.

[3] A. Rabis, P. Rodriguez, T.J. Schmidt, ACS Catal. 2 (2012) 864-890.

[4] N. Jung, D.Y. Chung, J. Ryu, S.J. Yoo, Y.E. Sung, Nano Today 9 (2014) 433-456.

[5] A. Morozan, B. Jousselme, S. Palacin, Energ. Environ. Sci. 4 (2011) 1238-1254.

[6] M. Shao, A. Peles, K. Shoemaker, Nano Lett. 11 (2011) 3714-3719.

[7] Y. Kang, M. Li, Y. Cai, M. Cargnello, R.E. Diaz, T.R. Gordon, N.L. Wieder, R.R. Adzic, R.J. Gorte, E.A. Stach, C.B. Murray, J. Am. Chem. Soc. 135 (2013) 2741-2747.

[8] K. Sasaki, H. Naohara, Y. Cai, Y.M. Choi, P. Liu, M.B. Vukmirovic, J.X. Wang, R.R. Adzic, Angew. Chem. Int. Edit. 49 (2010) 8602-8607.

[9] H. Yang, Angew. Chem. Int. Edit. 50 (2011) 2674-2676.

[10] Y.H. Bing, H.S. Liu, L. Zhang, D. Ghosh, J.J. Zhang, Chem. Soc. Rev. 39 (2010) 2184-2202.

[11] I.E.L. Stephens, A.S. Bondarenko, U. Gronbjerg, J. Rossmeisl, I. Chorkendorff, Energ. Environ. Sci. 5 (2012) 6744-6762.

[12] Y.J. Wang, D.P. Wilkinson, J.J. Zhang, Chem. Rev. 111 (2011) 7625-7651.

[13] S.M. Alia, G. Zhang, D. Kisailus, D. Li, S. Gu, K. Jensen, Y. Yan, Adv. Funct. Mater. 20 (2010) 3742-3746.

[14] Y.N. Xia, P.D. Yang, Y.G. Sun, Y.Y. Wu, B. Mayers, B. Gates, Y.D. Yin, F. Kim, Y.Q. Yan, Adv. Mater. 15 (2003) 353-389.

[15] L. Cademartiri, G.A. Ozin, Adv. Mater. 21 (2009) 1013-1020.

[16] J.T. Zhang, C.M. Li, Chem. Soc. Rev. 41 (2012) 7016-7031.

[17] C. Koenigsmann, W.P. Zhou, R.R. Adzic, E. Sutter, S.S. Wong, Nano Lett. 10 (2010) 2806-2811.

[18] C. Koenigsmann, S.S. Wong, Energ. Environ. Sci. 4 (2011) 1161-1176.

[19] B.Y. Xia, W.T. Ng, H.B. Wu, X. Wang, X.W. Lou, Angew. Chem. Int. Edit. 51 (2012) 7213-7216.

[20] W.C. Choi, S.I. Woo, J. Power Sources 124 (2003) 420-425.

[21] I.S. Park, J.H. Choi, Y.E. Sung, Electrochem. Solid St. 11 (2008) B71-B75.

[22] G.Y. Zhao, C.L. Xu, D.J. Guo, H. Li, H.L. Li, Appl. Surf. Sci. 253 (2007) 3242-3246.

[23] L.X. Ding, G.R. Li, Z.L. Wang, Z.Q. Liu, H. Liu, Y.X. Tong, Chem.-Eur. J. 18 (2012) 8386-8391.

[24] S.M. Choi, J.H. Kim, J.Y. Jung, E.Y. Yoon, W.B. Kim, Electrochim. Acta. 53 (2008) 5804-5811.

[25] Y. Lee, J. Kim, D.S. Yun, Y.S. Nam, Y. Shao-Horn, A.M. Belcher, Energ. Environ. Sci. 5 (2012) 8328-8334.

[26] X.F. Lu, C. Wang, Y. Wei, Small 5 (2009) 2349-2370.

[27] E.P. Lee, Z.M. Peng, W. Chen, S.W. Chen, H. Yang, Y.N. Xia, ACS Nano 2 (2008) 2167-2173.

[28] S. Du, Int. J. Low-Carbon Technol. 7 (2012) 44-54.

[29] M.E. Scofield, H.Q. Liu, S.S. Wong, Chem. Soc. Rev. 44 (2015) 5836-5860.

[30] J.Y. Chen, T. Herricks, M. Geissler, Y.N. Xia, J. Am. Chem. Soc. 126 (2004) 10854-10855.

[31] W. Du, D. Su, Q. Wang, A.I. Frenkel, X. Teng, Cryst. Growth Des. 11 (2011) 594-599.

[32] Z.Y. Zhang, M.J. Li, Z.L. Wu, W.Z. Li, Nanotechnology 22 (2011).

[33] S. Sun, D. Yang, G. Zhang, E. Sacher, J.P. Dodelet, Chem. Mater. 19 (2007) 6376-6378.

[34] S.H. Sun, D.Q. Yang, D. Villers, G.X. Zhang, E. Sacher, J.P. Dodelet, Adv. Mater. 20 (2008) 571-574.

[35] S. Sun, G. Zhang, D. Geng, Y. Chen, R. Li, M. Cai, X. Sun, Angew. Chem. 123 (2011) 442-446.

[36] S. Sun, G. Zhang, D. Geng, Y. Chen, M.N. Banis, R. Li, M. Cai, X. Sun, Chem.-Eur. J. 16 (2010) 829-835.

[37] A.C. Chen, P. Holt-Hindle, Chem. Rev. 110 (2010) 3767-3804.

[38] K.D. Gilroy, P. Farzinpour, A. Sundar, R.A. Hughes, S. Neretina, Chem. Mater. 26 (2014) 3340-3347.

[39] Y. Liu, D.G. Li, S.S. Sun, J. Mater. Chem. 21 (2011) 12579-12587.

[40] H. Zhang, M.S. Jin, Y.N. Xia, Chem. Soc. Rev. 41 (2012) 8035-8049.

[41] M.L. Calegaro, H.B. Suffredini, S.A.S. Machado, L.A. Avaca, J. Power Sources 156 (2006) 300-305.

[42] S. Bharathi, N. Fishelson, O. Lev, Langmuir 15 (1999) 1929-1937.

[43] M.R. Gao, J. Jiang, S.H. Yu, Small 8 (2012) 13-27.

[44] I. Katsounaros, S. Cherevko, A.R. Zeradjanin, K.J.J. Mayrhofer, Angew. Chem. Int. Edit. 53 (2014) 102-121.

[45] J. Greeley, I.E.L. Stephens, A.S. Bondarenko, T.P. Johansson, H.A. Hansen, T.F. Jaramillo, J. Rossmeisl, I. Chorkendorff, J.K. Norskov, Nat. Chem. 1 (2009) 552-556.

[46] N. Alonso-Vante, Chemphyschem 11 (2010) 2732-2744.

[47] S.J. Guo, S. Zhang, S.H. Sun, Angew. Chem. Int. Edit. 52 (2013) 8526-8544.

[48] V. Stamenkovic, B.S. Mun, K.J.J. Mayrhofer, P.N. Ross, N.M. Markovic, J. Rossmeisl, J. Greeley, J.K. Nørskov, Angew. Chem. 118 (2006) 2963-2967.

[49] J.K. Norskov, J. Rossmeisl, A. Logadottir, L. Lindqvist, J.R. Kitchin, T. Bligaard, H. Jonsson, J. Phys. Chem. B 108 (2004) 17886-17892.

[50] K. Jiang, H.X. Zhang, S.Z. Zou, W.B. Cai, Phys. Chem. Chem. Phys. 16 (2014) 20360-20376.

[51] Y. Liu, T.G. Kelly, J.G.G. Chen, W.E. Mustain, ACS Catal. 3 (2013) 1184-1194.

[52] Y. Xu, B. Zhang, Chem. Soc. Rev. 43 (2014) 2439-2450.

[53] Y. Li, Q. Wu, S. Jiao, C. Xu, L. Wang, Anal. Chem. 85 (2013) 4135-4140.

[54] S.J. Percival, B. Zhang, J. Phys. Chem. C 117 (2013) 13928-13935.

[55] Q. Xiao, M. Cai, M. Balogh, M. Tessema, Y. Lu, Nano Res. 5 (2012) 145-151.

[56] L.Y. Ruan, E.B. Zhu, Y. Chen, Z.Y. Lin, X.Q. Huang, X.F. Duan, Y. Huang, Angew. Chem. Int. Edit. 52 (2013) 12577-12581.

[57] A.B. Papandrew, R.W. Atkinson, G.A. Goenaga, S.S. Kocha, J.W. Zack, B.S. Pivovar, T.A. Zawodzinski, J. Electrochem. Soc. 160 (2013) F848-F852.

[58] S. Ci, J. Zou, G. Zeng, S. Luo, Z. Wen, J. Mater. Chem. 22 (2012) 16732-16737.

[59] G. Zhang, S. Sun, M. Cai, Y. Zhang, R. Li, X. Sun, Sci. Rep. 3 (2013) 1526.

[60] S.M. Alia, K. Jensen, C. Contreras, F. Garzon, B. Pivovar, Y. Yan, ACS Catal. 3 (2013) 358-362.

[61] W.J. Khudhayer, N.N. Kariuki, X.P. Wang, D.J. Myers, A.U. Shaikh, T. Karabacak, J. Electrochem. Soc. 158 (2011) B1029-B1041.

[62] J. Xu, G. Fu, Y. Tang, Y. Zhou, Y. Chen, T. Lu, J. Mater. Chem. 22 (2012) 13585-13590.

[63] G. Fu, X. Jiang, M. Gong, Y. Chen, Y. Tang, J. Lin, T. Lu, Nanoscale (2014).

[64] T.T.H. Van, C.J. Pan, J. Rick, W.N. Su, B.J. Hwang, J. Am. Chem. Soc. 133 (2011) 11716-11724.

[65] W. Shimizu, K. Okada, Y. Fujita, S. Zhao, Y. Murakami, J. Power Sources 205 (2012) 24-31.

[66] R. Wu, Y. Xue, X. Qian, H. Liu, K. Zhou, S.H. Chan, J.N. Tey, J. Wei, B. Zhu, Y. Huang, Int. J. Hydrogen Energy 38 (2013) 16677-16684.

[67] V.T.T. Ho, N.G. Nguyen, C.J. Pan, J.H. Cheng, J. Rick, W.N. Su, J.F. Lee, H.S. Sheu, B.J. Hwang, Nano Energy 1 (2012) 687-695.

[68] S.C. Sahu, A.K. Samantara, B. Satpati, S. Bhattacharjee, B.K. Jena, Nanoscale 5 (2013) 11265-11274.

[69] R. Wang, D.C. Higgins, M.A. Hoque, D. Lee, F. Hassan, Z. Chen, Sci. Rep. 3 (2013) 2431.

[70] J.N. Tiwari, K.C. Kemp, K. Nath, R.N. Tiwari, H.G. Nam, K.S. Kim, ACS Nano 7 (2013) 9223-9231.

[71] W.T. Yu, M.D. Porosoff, J.G.G. Chen, Chem. Rev. 112 (2012) 5780-5817.

[72] C. Koenigsmann, M.E. Scofield, H. Liu, S.S. Wong, J. Phy. Chem. Lett. 3 (2012) 3385-3398.

[73] R. Carrera-Cerritos, V. Baglio, A.S. Aricò, J. Ledesma-García, M.F. Sgroi, D. Pullini, A.J. Pruna, D.B. Mataix, R. Fuentes-Ramírez, L.G. Arriaga, Appl. Catal. B-Environ.144 (2014) 554-560.

[74] Z. Zhang, L. Xin, K. Sun, W. Li, Int. J. Hydrogen Energy 36 (2011) 12686-12697.

[75] Z. Zhu, Y. Zhai, C. Zhu, Z. Wang, S. Dong, Electrochem. Commun. 36 (2013) 22-25.

[76] Y.Z. Lu, Y.Y. Jiang, W. Chen, Nano Energy 2 (2013) 836-844.

[77] T.H. Yeh, C.W. Liu, H.S. Chen, K.W. Wang, Electrochem. Commun. 31 (2013) 125-128.

[78] Y.C. Tseng, H.S. Chen, C.W. Liu, T.H. Yeh, K.W. Wang, J. Mater. Chem. A 2 (2014) 4270-4275.

[79] Y.T. Liang, S.P. Lin, C.W. Liu, S.R. Chung, T.Y. Chen, J.H. Wang, K.W. Wang, Chem. Commun. 51 (2015) 6605-6608.

[80] Y.T. Liang, C.W. Liu, H.S. Chen, T.J. Lin, C.Y. Yang, T.L. Chen, C.H. Lin, M.C. Tu, K.W. Wang, RSC Adv. 5 (2015) 39205-39208.

[81] Z. Duan, G. Wang, Phy. Chem. Chem. Phy.13 (2011) 20178-20187.

[82] J.I. Shui, C. Chen, J.C.M. Li, Adv. Funct. Mater. 21 (2011) 3357-3362.

[83] Z. Zhang, M. Li, Z. Wu, W. Li, Nanotechnology 22 (2011) 015602.

[84] S.J. Guo, D.G. Li, H.Y. Zhu, S. Zhang, N.M. Markovic, V.R. Stamenkovic, S.H. Sun, Angew. Chem. Int. Edit. 52 (2013) 3465-3468.

[85] J.A. Wittkopf, J. Zheng, Y.S. Yan, ACS Catal. 4 (2014) 3145-3151.

[86] N.N. Kariuki, W.J. Khudhayer, T. Karabacak, D.J. Myers, ACS Catal. 3 (2013) 3123-3132.

[87] X.F. Lu, M. McKiernan, Z.M. Peng, E.P. Lee, H. Yang, Y.N. Xia, Sci Adv. Mater. 2 (2010) 413-420.

[88] L. Su, S. Shrestha, Z. Zhang, W. Mustain, Y. Lei, J. Mater. Chem. A 1 (2013) 12293-12301.

[89] M. Mohl, D. Dobo, A. Kukovecz, Z. Konya, K. Kordas, J. Wei, R. Vajtai, P.M. Ajayan, J. Phy. Chem. C 115 (2011) 9403-9409.

[90] C.H. Cui, H.H. Li, X.J. Liu, M.R. Gao, S.H. Yu, ACS Catal. 2 (2012) 916-924.

[91] S.W. Chou, J.J. Shyue, C.H. Chien, C.C. Chen, Y.Y. Chen, P.T. Chou, Chem. Mater. 24 (2012) 2527-2533.

[92] H. Zhu, S. Zhang, S. Guo, D. Su, S. Sun, J. Am. Chem. Soc. 135 (2013) 7130-7133.

[93] L.C. Liu, G. Samjeske, S. Takao, K. Nagasawa, Y. Lwasawa, J. Power Sources 253 (2014) 1-8.

[94] H.H. Li, C.H. Cui, S. Zhao, H.B. Yao, M.R. Gao, F.J. Fan, S.H. Yu, Adv. Energy. Mater. 2 (2012) 1182-1187.

[95] L. Liu, E. Pippel, Angew. Chem. Int. Edit. 50 (2011) 2729-2733.

[96] X. Liu, D. Wang, Y. Li, Nano Today 7 (2012) 448-466.

[97] M. Oezaslan, F. Hasché, P. Strasser, J. Phy. Chem. Lett. 4 (2013) 3273-3291.

[98] S.J. Hwang, S.J. Yoo, J. Shin, Y.H. Cho, J.H. Jang, E. Cho, Y.E. Sung, S.W. Nam, T.H. Lim, S.C. Lee, S.K. Kim, Sci. Rep. 3 (2013) 1309.

[99] C. Koenigsmann, A.C. Santulli, K. Gong, M.B. Vukmirovic, W.P. Zhou, E. Sutter, S.S. Wong, R.R. Adzic, J. Am. Chem. Soc. 133 (2011) 9783-9795.

[100] M.A. Bromley, C. Boxall, Electrochem. Commun. 23 (2012) 87-89.

[101] K. Gong, J. Park, D. Su, R.R. Adzic, J. Solid State Electrochem. 18 (2014) 1171-1179.

[102] S.M. Alia, K.O. Jensen, B.S. Pivovar, Y. Yan, ACS Catal. 2 (2012) 858-863.

[103] H. Naohara, Y. Okamoto, N. Toshima, J. Power Sources 196 (2011) 7510-7513.

[104] H.Q. Liu, W. An, Y.Y. Li, A.I. Frenkel, K. Sasaki, C. Koenigsmann, D. Su, R.M. Anderson, R.M. Crooks, R.R. Adzic, P. Liu, S.S. Wong, J. Am. Chem. Soc. 137 (2015) 12597-12609.

[105] C.W. Liu, Y.C. Wei, C.C. Liu, K.W. Wang, J. Mater. Chem. 22 (2012) 4641-4644.

[106] S. Guo, S. Zhang, D. Su, S. Sun, J. Am. Chem. Soc. 135 (2013) 13879-13884.

[107] Y.M. Tan, J.M. Fan, G.X. Chen, N.F. Zheng, Q.J. Xie, Chem. Commun. 47 (2011) 11624-11626.

[108] B. Lim, M. Jiang, T. Yu, P.C. Camargo, Y. Xia, Nano Res. 3 (2010) 69-80.

[109] S. Ghosh, S. Mondal, C. Retna Raj, J. Mater. Chem. A 2 (2014) 2233-2239.

[110] H.B. Liao, Y.L. Hou, Chem. Mater. 25 (2013) 457-465.

[111] C. Koenigsmann, A.C. Santulli, E. Sutter, S.S. Wong, ACS Nano 5 (2011) 7471-7487.

[112] X. Teng, W.Q. Han, W. Ku, M. Hücker, Angew. Chem. 120 (2008) 2085-2088.

[113] S.M. Alia, K. Duong, T. Liu, K. Jensen, Y. Yan, Chemsuschem (2014) 1739-1744.

[114] F.J. Yu, W.Z. Zhou, R.M. Bellabarba, R.P. Tooze, Nanoscale 6 (2014) 1093-1098.

[115] Z. Zhang, K.L. More, K. Sun, Z. Wu, W. Li, Chem. Mater. 23 (2011) 1570-1577.

[116] W. Sun, A. Hsu, R.R. Chen, J. Power Sources 196 (2011) 4491-4498.

[117] X.R. Li, X.L. Li, M.C. Xu, J.J. Xu, H.Y. Chen, J. Mater. Chem. A 2 (2014) 1697-1703.

[118] C. Koenigsmann, E. Sutter, T.A. Chiesa, R.R. Adzic, S.S. Wong, Nano Lett. 12 (2012) 2013-2020.

[119] C. Koenigsmann, E. Sutter, R.R. Adzic, S.S. Wong, J. Phy. Chem. C 116 (2012) 15297-15306.

[120] A. Cha, J.H. Shim, A. Jo, S.C. Lee, Y. Lee, C. Lee, Electroanal. 26 (2014) 723-731.

[121] Z.L. Gengtao Fu, Yu Chen, Jun Lin, Yawen Tang, Tianhong Lu, Nano Res. 7 (2014) 1205-1214.

[122] N. Wang, X. Cao, Q. Chen, G. Lin, Chem.-Eur. J. 18 (2012) 6049-6054.

[123] Y.Z. Lu, Y.C. Wang, W. Chen, J. Power Sources 196 (2011) 3033-3038.

[124] B. Kim, Y. Choi, S.Y. Cho, Y.S. Yun, H.J. Jin, J. Nanosci. Nanotechno. 13 (2013) 7454-7458.

[125] D. Yu, J. Yao, L. Qiu, Y. Wu, L. Li, Y. Feng, Q. Liu, D. Li, H. Wang, RSC Adv. 3 (2013) 11552-11555.

[126] M. Han, S. Liu, L. Zhang, C. Zhang, W. Tu, Z. Dai, J. Bao, ACS Appl. Mater. Inter. 4 (2012) 6654-6660.

[127] J.H. Shim, J. Yang, S.J. Kim, C. Lee, Y. Lee, J. Mater. Chem. 22 (2012) 15285-15290.

[128] Z. Wen, S. Ci, F. Zhang, X. Feng, S. Cui, S. Mao, S. Luo, Z. He, J. Chen, Adv. Mater. 24 (2012) 1399-1404.

[129] S. Liu, Z. Zhang, J. Bao, Y. Lan, W. Tu, M. Han, Z. Dai, J. Phy. Chem. C 117 (2013) 15164-15173.

[130] Z. Yang, X.M. Zhou, H.G. Nie, Z. Yao, S.M. Huang, ACS Appl. Mater. Inter. 3 (2011) 2601-2606.

[131] T.N. Lambert, D.J. Davis, W. Lu, S.J. Limmer, P.G. Kotula, A. Thuli, M. Hungate, G.D. Ruan, Z. Jin, J.M. Tour, Chem. Commun. 48 (2012) 7931-7933.

[132] J. Du, Y.D. Pan, T.R. Zhang, X.P. Han, F.Y. Cheng, J. Chen, J. Mater. Chem. 22 (2012) 15812-15818.

[133] C. Jin, F.L. Lu, X.C. Cao, Z.R. Yang, R.Z. Yang, J. Mater. Chem. A 1 (2013) 12170-12177.

[134] T. Fujigaya, T. Uchinoumi, K. Kaneko, N. Nakashima, Chem. Commun. 47 (2011) 6843-6845.

[135] A. Zhao, J. Masa, W. Schuhmann, W. Xia, J. Phy. Chem. C 117 (2013) 24283-24291.

[136] G. Tuci, C. Zafferoni, P. D'Ambrosio, S. Caporali, M. Ceppatelli, A. Rossin, T. Tsoufis, M. Innocenti, G. Giambastiani, ACS Catal. 3 (2013) 2108-2111.

[137] H. Huang, D. Sun, X. Wang, J. Phy. Chem. C 115 (2011) 19405-19412.

[138] S. Wang, S.P. Jiang, X. Wang, J. Guo, Electrochim. Acta. 56 (2011) 1563-1569.

[139] L. Wang, H. Wang, Y. Nemoto, Y. Yamauchi, Chem. Mater. 22 (2010) 2835-2841.

[140] B.Y. Xia, H.B. Wu, Y. Yan, X.W. Lou, X. Wang, J. Am. Chem. Soc. 135 (2013) 9480-9485.

[141] Y. Kim, H.J. Kim, Y.S. Kim, S.M. Choi, M.H. Seo, W.B. Kim, J. Phy. Chem. C 116 (2012) 18093-18100.

[142] L. Wei, Y.J. Fan, H.H. Wang, N. Tian, Z.Y. Zhou, S.G. Sun, Electrochim. Acta. 76 (2012) 468-474.

[143] Y.B. He, G.R. Li, Z.L. Wang, Y.N. Ou, Y.X. Tong, J. Phy. Chem. C 114 (2010) 19175-19181.

[144] C. Li, T. Sato, Y. Yamauchi, Angew. Chem. Int. Edit. 52 (2013) 8050-8053.

[145] H. Meng, F.Y. Xie, J. Chen, S.H. Sun, P.K. Shen, Nanoscale 3 (2011) 5041-5048.

[146] F. Si, L. Ma, C. Liu, X. Zhang, W. Xing, RSC Adv. 2 (2012) 401-403.

[147] Rajesh, R.K. Paul, A. Mulchandani, J. Power Sources 223 (2013) 23-29.

[148] R. Wang, D.C. Higgins, M.A. Hoque, D. Lee, F. Hassan, Z. Chen, Sci. Rep. 3 (2013) 2341.

[149] Z.M. Luo, L.H. Yuwen, B.Q. Bao, J. Tian, X.R. Zhu, L.X. Weng, L.H. Wang, J. Mater. Chem. 22 (2012) 7791-7796.

[150] S. Du, Y. Lu, S.K. Malladi, Q. Xu, R. Steinberger-Wilckens, J. Mater. Chem. A 2 (2014) 692-698.

[151] J.J. Lv, J.N. Zheng, S.S. Li, L.L. Chen, A.J. Wang, J.J. Feng, J. Mater. Chem. A 2 (2014) 4384-4390.

[152] C. Zhu, S. Guo, S. Dong, Adv. Mater. 24 (2012) 2326-2331.

[153] C. Koenigsmann, S.S. Wong, ACS Catal. 3 (2013) 2031-2040.

[154] L.X. Ding, C.L. Liang, H. Xu, A.L. Wang, Y.X. Tong, G.R. Li, Adv. Mater. Inter. (2014) 1400005.

[155] S.S. Li, J.N. Zheng, X. Ma, Y.Y. Hu, A.J. Wang, J.R. Chen, J.J. Feng, Nanoscale 6 (2014) 5708-5713.

[156] M. Xiao, S. Li, J. Zhu, K. Li, C. Liu, W. Xing, Chempluschem 79 (2014) 1123-1128.

[157] L. Chen, L. Kuai, X. Yu, W. Li, B. Geng, Chem.-Eur. J. 19 (2013) 11753-11758.

[158] Q. Yuan, Z. Zhou, J. Zhuang, X. Wang, Chem. Mater. 22 (2010) 2395-2402.

[159] B. Li, D.C. Higgins, S.M. Zhu, H. Li, H.J. Wang, J.X. Ma, Z.W. Chen, Catal. Commun. 18 (2012) 51-54.

[160] Y.W. Lee, B.Y. Kim, K.H. Lee, W.J. Song, G.Z. Cao, K.W. Park, Int. J. Electrochem. Sci. 8 (2013) 2305-2312.

[161] E. Bertin, S. Garbarino, A. Ponrouch, D. Guay, J. Power Sources 206 (2012) 20-28.

[162] X.F. Yu, D.S. Wang, Q. Peng, Y.D. Li, Chem.-Eur. J. 19 (2013) 233-239.

[163] H. Qiu, L. Li, Q. Lang, F. Zou, X. Huang, RSC Adv. 2 (2012) 3548.

[164] X.Y. Zhang, D. Li, D.H. Dong, H.T. Wang, P.A. Webley, Mater. Lett. 64 (2010) 1169-1172.

[165] B.M. Luo, X.B. Yan, S. Xu, Q.J. Xue, Electrochem. Commun. 30 (2013) 71-74.

[166] L.X. Ding, A.L. Wang, G.R. Li, Z.Q. Liu, W.X. Zhao, C.Y. Su, Y.X. Tong, J. Am. Chem. Soc. 134 (2012) 5730-5733.

[167] P. Wu, H. Zhang, Y. Qian, Y. Hu, H. Zhang, C. Cai, J. Phy. Chem. C 117 (2013) 19091-19100.

[168] S. Guo, S. Zhang, X. Sun, S. Sun, J. Am. Chem. Soc. 133 (2011) 15354-15357.

[169] H.H. Li, S. Zhao, M. Gong, C.H. Cui, D. He, H.W. Liang, L. Wu, S.H. Yu, Angew. Chem. Int. Edit. 52 (2013) 7472-7476.

[170] C. Zhu, S. Guo, S. Dong, J. Mater. Chem. 22 (2012) 14851-14855.

[171] C. Du, M. Chen, W. Wang, Q. Tan, K. Xiong, G. Yin, J. Power Sources 240 (2013) 630-635.

[172] Z.Y. Huang, H.H. Zhou, Y.W. Chang, C.P. Fu, F.Y. Zeng, Y.F. Kuang, Chem. Phys. Lett. 585 (2013) 128-132.

[173] C. Koenigsmann, D.B. Semple, E. Sutter, S.E. Tobierre, S.S. Wong, ACS Appl. Mater. Inter. 5 (2013) 5518-5530.

[174] L.X. Ding, G.R. Li, Z.L. Wang, Z.Q. Liu, H. Liu, Y.X. Tong, Chem.-Eur. J. 18 (2012) 8386-8391.

[175] L. Wang, Y. Nemoto, Y. Yamauchi, J. Am. Chem. Soc. 133 (2011) 9674-9677.

[176] F. Lan, D.L. Wang, S.F. Lu, J. Zhang, D.W. Liang, S.K. Peng, Y.Y. Liu, Y. Xiang, J. Mater. Chem. A 1 (2013) 1548-1552.

[177] M. Ren, L. Zou, T. Yuan, Q. Huang, Z. Zou, X. Li, H. Yang, J. Power Sources 267 (2014) 527-532.

[178] W. Hong, J. Wang, E. Wang, Int. J. Hydrogen Energy 39 (2014) 3226-3230.

[179] J. Wang, Y. Chen, H. Liu, R. Li, X. Sun, Electrochem. Commun. 12 (2010) 219-222.

[180] Y. Wang, S.I. Choi, X. Zhao, S. Xie, H.C. Peng, M. Chi, C.Z. Huang, Y. Xia, Adv. Funct. Mater. 24 (2014) 131-139.

[181] J.N. Zheng, M. Zhang, F.F. Li, S.S. Li, A.J. Wang, J.J. Feng, Electrochim. Acta. 130 (2014) 446-452.

[182] H. Meng, C.X. Wang, P.K. Shen, G. Wu, Energ. Environ. Sci. 4 (2011) 1522-1526.

[183] A.L. Wang, H. Xu, J.X. Feng, L.X. Ding, Y.X. Tong, G.R. Li, J. Am. Chem. Soc. 135 (2013) 10703-10709.

[184] Y.W. Lee, M. Kim, Y. Kim, S.W. Kang, J.-H. Lee, S.W. Han, J. Phy. Chem. C 114 (2010) 7689-7693.

[185] L. Shi, A. Wang, T. Zhang, B. Zhang, D. Su, H. Li, Y. Song, J. Phy. Chem. C 117 (2013) 12526-12536.

[186] H. Wang, Z. Sun, Y. Yang, D. Su, Nanoscale 5 (2013) 139-142.

[187] W. Hong, J. Wang, E. Wang, ACS Appl. Mater. Inter. 6 (2014) 9481-9487.

[188] Y. Lu, W. Chen, ACS Catal. 2 (2011) 84-90.

[189] Y. Lu, W. Chen, J. Phy. Chem. C 114 (2010) 21190-21200.

[190] S. Shen, T. Zhao, J. Mater. Chem. A 1 (2013) 906-912.

[191] C. Du, M. Chen, W. Wang, G. Yin, ACS Appl. Mater. Inter. 3 (2010) 105-109.

[192] H.B. Liao, J.H. Zhu, Y.L. Hou, Nanoscale 6 (2014) 1049-1055.

[193] R.M. Ding, J.P. Liu, J. Jiang, F. Wu, J.H. Zhu, X.T. Huang, Catal. Sci. Technol. 1 (2011) 1406-1411.

[194] A.L. Wang, H.C. Wan, H. Xu, Y.X. Tong, G.R. Li, Electrochim. Acta. 127 (2014) 448-453.

[195] H.W. Liang, X.A. Cao, F. Zhou, C.H. Cui, W.J. Zhang, S.H. Yu, Adv. Mater. 23 (2011) 1467-1471.

[196] B. Li, Z. Yan, D.C. Higgins, D. Yang, Z. Chen, J. Ma, J. Power Sources 262 (2014) 488-493.

[197] M.T. Sung, M.H. Chang, M.H. Ho, J. Power Sources 249 (2014) 320-326.

[198] B. Li, D.C. Higgins, Q.F. Xiao, D.J. Yang, C.M. Zhng, M. Cai, Z.W. Chen, J.X. Ma, Appl. Catal. B-Environ. 162 (2015) 133-140.

[199] W.H. Lee, H. Kim, Int. J. Hydrogen Energy 38 (2013) 7126-7132.

[200] S. Holdcroft, Chem. Mater. 26 (2014) 381-393.

[201] M.K. Debe, Nature 486 (2012) 43-51.

[202] M.K. Debe, ECS Trans. 45 (2012) 47-68.

[203] D.A. Cullen, M. Lopez-Haro, P. Bayle-Guillemaud, L. Guetaz, M.K. Debe, A.J. Steinbach, J. Mater. Chem. A 3 (2015) 11660-11667.

[204] S.F. Du, J. Power Sources 195 (2010) 289-292.

[205] S.F. Du, B.G. Pollee, Int. J. Hydrogen Energ 37 (2012) 17892-17898.

[206] S.F. Du, B. Millington, B.G. Pollet, Int. J. Hydrogen Energy 36 (2011) 4386-4393.

[207] S. Sui, X.L. Zhuo, K.H. Su, X.Y. Yao, J.L. Zhang, S.F. Du, K. Kendall, J. Energy Chem. 22 (2013) 477-483.

[208] Y. Lu, S. Du, R. Steinberger-Wilckens, Appl. Catal. B-Environ.164 (2015) 389-395.

[209] H.A. Gasteiger, S.S. Kocha, B. Sompalli, F.T. Wagner, Appl. Catal. B-Environ. 56 (2005) 9-35.

[210] S.F. Du, K.J. Lin, S.K. Malladi, Y.X. Lu, S.H. Sun, Q. Xu, R. Steinberger-Wilckens, H.S. Dong, Sci. Rep. 4 (2014) 6439.

[211] B. Lim, M.J. Jiang, P.H.C. Camargo, E.C. Cho, J. Tao, X.M. Lu, Y.M. Zhu, Y.N. Xia, Science 324 (2009) 1302-1305.

[212] Y. Lu, S. Du, R. Steinberger-Wilckens, Appl. Catal. B-Environ.187 (2016) 108-114.

[213] X.Y. Yao, K.H. Su, S. Sui, L.W. Mao, A. He, J.L. Zhang, S.F. Du, Int. J. Hydrogen Energy 38 (2013) 12374-12378.

[214] K. Su, S. Sui, X. Yao, Z. Wei, J. Zhang, S. Du, Int. J. Hydrogen Energy 39 (2014) 3397-3403.

[215] Z. Wei, K. Su, S. Sui, A. He, S. Du, Int. J. Hydrogen Energy 40 (2015) 3068-3074.

[216] F. Xia, L. Jiang, Adv. Mater. 20 (2008) 2842-2858.

[217] G. Fu, X. Jiang, M. Gong, Y. Chen, Y. Tang, J. Lin, T. Lu, Nanoscale 6 (2014) 8226-8234.

[218] G.T. Fu, K. Wu, J. Lin, Y.W. Tang, Y. Chen, Y.M. Zhou, T.H. Lu, J. Phys. Chem. C 117 (2013) 9826-9834.

[219] D.J. Guo, S.K. Cui, D. Cheng, P. Zhang, L. Jiang, C.C. Zhang, J. Power Sources 255 (2014) 157-162.

[220] G. Tuci, C. Zafferoni, P. D'Ambrosio, S. Caporali, M. Ceppatelli, A. Rossin, T. Tsoufis, M. Innocenti, G. Giambastiani, ACS Catal. 3 (2013) 2108-2111.

[221] J.S. Lee, G.S. Park, H.I. Lee, S.T. Kim, R.G. Cao, M.L. Liu, J. Cho, Nano Lett. 11 (2011) 5362-5366.

[222] S.H. Chun, H.-A. Choi, M. Kang, M. Koh, N.-S. Lee, S.C. Lee, M. Lee, Y. Lee, C. Lee, M.H. Kim, ACS Appl. Mater. Inter. 5 (2013) 8401-8406.

Figure Captions:

Fig. 1 Volcano plot for ORR activity of (a) pure metal and (b) Pt-based transition metal alloys versus the oxygen binding energy (ΔE_O). Adapted from ref. [45, 49] with permission from ACS Publications and Nature Publishing Group.

Fig. 2 The polarization curve (a) for the acid-washed ultrathin platinum nanowires as compared with commercial 3.3 nm platinum nanoparticles 46.4 wt % on a Vulcan carbon support, both on a glassy carbon rotating disk electrode. Curves (anodic sweep direction) were obtained with a rotation rate of 1600 rpm in a 0.1 M $HClO_4$ solution at 20 °C. (b) The electrochemical surface area (ECSA) activity at 0.9 V for acid-treated ultrathin nanowires (red) as compared with commercial supported nanoparticles (green), acid-treated platinum nanoparticles (orange), previously synthesized platinum nanotubes (black), and as-prepared ultrathin nanowires without acid treatment (blue), respectively. Adapted from ref. [17] with permission from ACS Publications.

Fig. 3 (a, b) SEM, (c) TEM and (d) high resolution TEM images of SG-PtNW-3 catalyst. Insets in (d) are the Fourier filtered high resolution TEM images of the areas highlighted by the dashed yellow squares. Adapted from ref. [69] with permission from Nature Publishing Group.

Fig. 4 (a) PtCu tube after annealing at 600 °C. (b) CuPt restructured tube obtained after 250 potential cycles. Insets are the ED patterns showing the order-disorder transformation before and after morphology restructuring. (c) Amplified TEM image shows the highly rough surface. (d) Schematic of surface evolution after potential cycles. Adapted from ref. [90] with permission from ACS Publications.

Fig. 5 (a,b) TEM images showing the morphological evolution of Pd-Pt nanodendrites. High-resolution TEM images of (c) an individual Pd-Pt particle and (d) the small Pt particles shown in (a). In (c), the Pt bumps on the Pd seed are indicated by arrows. (e) High-resolution TEM image of a single Pd-Pt nanodendrite. It can be seen that the lattice fringes are coherently extended from the Pd core to the Pt branches. (f) High-resolution TEM image taken from a Pt branch containing a single twin plane in its structure and the corresponding Fourier transform (FT) pattern (inset). A twin plane is indicated by tw. Adapted from ref. [108] with permission from Springer.

Fig. 6 Schematic diagram for the MnO_x-CNT ORR mechanism. Adapted from ref. [130] with permission from ACS Publications.

Fig. 7 (a) SEM and (b) TEM images of the PtAu NT. (c) Low-magnification HRTEM image of the PtAu NT and (d) the corresponding high-magnification HRTEM image of panel c. The insets of panels b and c show the STEM image with the EDS line scan and the SAED pattern of the PtAu NT, respectively. Adapted from ref. [141] with permission from ACS Publications.

Fig. 8 (a) TEM image of the dispersive nanocrystals after ultrasonic dispersion of PtPd porous hollow nanorod arrays (PHNRAs); (b) HAADF-STEM image of the dispersive nanocrystals after ultrasonic dispersion of PtPd PHNRAs; (c) CVs measured in 0.5 M CH_3OH+0.5 M H_2SO_4 at 50 mV/s; (d) Chronoamperometry curves measured in 0.5 M H_2SO_4+0.5 M CH_3OH at 50 mV/s (The corresponding potential was held at 0.75 V for the PtPd PHNRAs and 0.60 V for the commercial Pt/C and PtPd film, respectively, during the measurements); (e) Schematic illustration for the advantages of PHNRAs as catalysts. Adapted from ref. [154] with permission from Wiley.

Fig. 9 (a) SEM image of Pt-Ni-P nanotube arrays (NTAs); (b) Scheme for the almost complete oxidation of carbonaceous species generated during methanol electrooxidation in

the porous walls of Pt-Ni-P NTAs; (c) CVs of Pt-Ni-P and Pt-Ni NTAs in 0.5 M CH_3OH+0.5 M H_2SO_4 at 50 mV/s; (d) Chronoamperometry curves of Pt-Ni-P and Pt-Ni NTAs in 0.5 M H_2SO_4+0.5 M CH_3OH at 50 mV/s. Adapted from ref. [166] with permission from ACS Publications.

Fig. 10 (a) TEM images of Au-Pt core-shell NWs of 1:1 atomic ratio after the formation of Pt shell clearly show the different morphologies and increase in diameter sizes. (b) The co-existence of Au and Ag as core (simply called as Au core) and Pt as shells were confirmed. Adapted from ref. [25] with permission from RSC.

Fig. 11 Average cell power as a function of the operation time, (A) PtNW/C and (C) commercial Pt/C; I–V and I–P curves of (B) PtNW/C and (D) commercial Pt/C. Adapted from ref. [198] with permission from Elsevier.

Fig. 12 SEM images of the PtCoMn alloy catalyst sputter coating on the microstructured substrate supported whiskers for the fabrication of NSTF catalyst elecgtrodes. Adapted from ref. [202] with permission from ECS Publications.

Fig. 13 Images of Pt nanowires grown on ASPN-treated GDLs. (a-c) SEM images of a 3D nano-architectured catalyst layer with Pt-nanowire arrays in-situ grown on the treated GDL support surface, at three different magnifications. The support area is 5 cm^2. (d-f) TEM and HR-TEM images of Pt nanowires in the nano-architectured catalyst layer. (f) shows a HR-TEM image of the part specified by the white square in (e), indicating the single-crystal nanowires with the growth direction along the <111> axis. Adapted from ref. [210] with permission from Nature Publishing Group.